Image Reconstruction for a Hand-held Low-Field MRI Scanner via Deep Learning

A.E. Bekkering

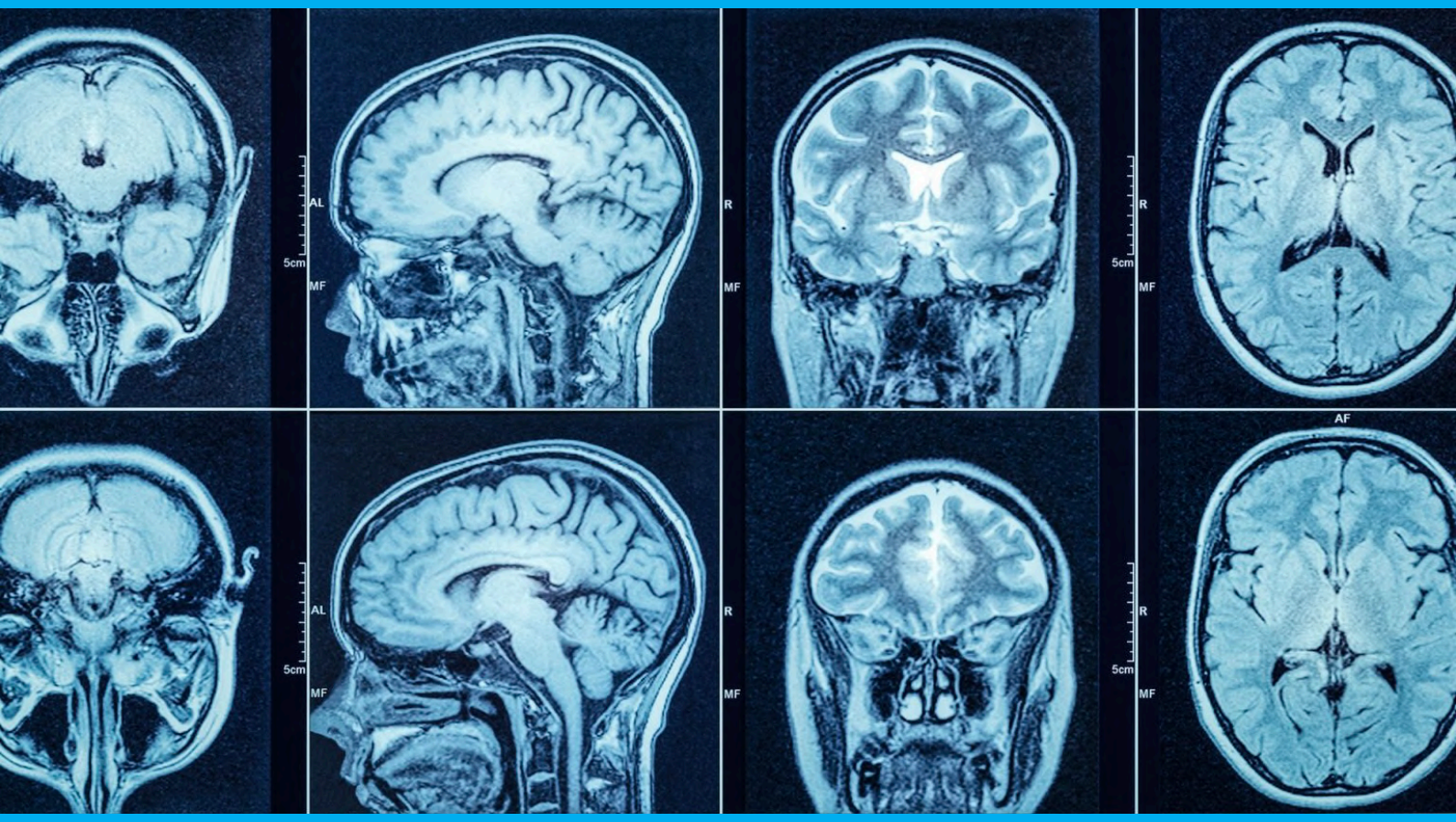

TU Delft

Image Reconstruction for a Handheld Low-Field MRI Scanner via Deep Learning

by

A.E. Bekkering

to obtain the degree of Master of Science
in Biomedical Engineering
at the Delft University of Technology.

Student number: 4389395

Thesis committee:	Dr. ir. R. F. Remis,	TU Delft, Chair
	Prof. dr. ir. M. B. van Gijzen,	TU Delft, Daily supervisor
	Dr. F. M. Vos,	TU Delft

TU Delft

Abstract

MRI has been used worldwide as an imaging modality for decades due to its ability to distinguish between soft tissues. However, MRIs cannot be used in all situations due to their extensive hard- and software. For this reason, research in the field of low-field MRI has been conducted. Low-field MRI systems do not use superconducting magnets but restive, or in this research, permanent magnets. This reduces the costs of these scanners, but these same changes result in a poorer signal-to-noise ratio (SNR) than high-field scanners. Based on this hardware, research in single-sided scanners has emerged, and various research groups have been able to reconstruct images with these scanners. They are based on conventional MRI hardware including a radiofrequency (RF) coil, permanent magnets and gradients coils for encoding. In collaboration with the Technical University (TU) Delft, a handheld scanner has been constructed in the Leiden University Medical Center (LUMC). This scanner consists of an RF coil and a permanent magnet and does not have a gradient coil. The inhomogeneity of the B_0 can be used for spatially encoding the signal based on translations. The SNR in images is improved with model-based image reconstruction. Although, in theory, this set-up should work, the image results so far have been somewhat disappointing. Therefore, in this thesis, we have investigated a different approach, using a neural network. In this research, the correlation between the received signal of a measurement and a simulation of the same shape is found to be greater than the correlation between other simulations and the received signal. Due to this proven correlation, an image reconstruction deep learning algorithm is constructed based on the AUTOMAP model. Simulated signals are reconstructed into images with promising results; however, the algorithm cannot reconstruct measured data. Therefore, suggestions for future improvement include improving the simulated data set and adding more real measurements that would allow for training on a measured data set.

Preface

With this thesis '*Image Reconstruction for a Handheld Low-field MRI Scanner via Deep Learning*', my academic period comes to an end.

After a bachelor's in Medical Natural Sciences at the Vrije Universiteit Amsterdam and my bachelor's project in the VUMC, I knew I wanted to combine engineering challenges with a human element. This marked the start of my master's in Biomedical Engineering, focusing on Medical Physics. When I started this project, we were well into a year of Covid-19. Even though only the first month of my master's was on campus, working from home and endless teams and zoom meetings never really felt normal. I would not have been able to finish this thesis without my outstanding support system.

Firstly I want to thank Martin for his endless optimism. Your ability to always look at the bright side of life, especially in this project, kept my spirit up. Thank you for, despite your busy schedule, always finding the time for me. Then I would like to thank Rob for his expertise and guidance. Your contributions made this a complete story in the last phase of the project. Thanks to Merel, to whom I could go with all my questions, and Danny, who helped me with all the hardware troubles I faced.

Furthermore, thanks go out to the Applied Research department of Medis Medical Imaging for showing me the relevance of medical imaging research in practice. A special thanks to everyone from the Deep Learning department who guided me in my first deep learning project and to whom I could still turn with questions in this project.

And lastly, I would like to thank my friends and family. My friends and roommates were there to distract me from my research when I needed to clear my head, go for a walk when I needed some fresh air, and cook me dinner when I had to work on this project till late. Thanks to Joost for always listening to me talking about medical imaging, deep learning and other engineering subjects. Your endless patience keeps me grounded. Thanks to my Dad, whose fault it might be that I ended up studying in Delft, and to my Mom, who would have been very proud of this milestone.

A.E. Bekkering
Delft, May 2022

Contents

List of Figures

List of Tables

1 Introduction

Since the first X-ray image of a body part was made in 1895 by Röntgen, the importance of medical imaging has increased significantly. After X-ray imaging, in which mainly the difference between bone and soft tissue can be distinguished, other imaging modalities arose, such as Positron Emission Tomography (PET), Computer Tomography (CT) and Magnetic Resonance Imaging (MRI). This last imaging modality has grown immensely in the past few decades due to its ability to distinguish between different soft tissues. Increasing field strengths have resulted in higher sensitivity and resolution. While this increase in sensitivity and resolution has great clinical use, this high field strength is not applicable in all situations. In this chapter, the history and basics of MRI are discussed, after which low-field and handheld MRI is introduced. Finally, artificial intelligence in medical imaging is discussed. All this leads to the research question in this project.

1.1. Magnetic Resonance Imaging

In 1952 Felix Bloch and Edward Mills Purcell won the Nobel Prize in physics ”for their development of new methods for nuclear magnetic precision measurements and discoveries in connection therewith” [25]. Until the 1970’s research in nuclear spin resonance was focused on physics or chemistry. However, in the seventies, research emerged in which the idea of nuclear spin resonance for an imaging modality was explored. The amount of research increased when the ability to distinguish between tumour and healthy tissue was introduced by Damadian in 1971 [12].

In the 1970s, it was believed that it would not be possible to use a magnet strength higher than 0.5 Tesla (T) due to the physical effects of the magnetic field on the body. However, a scanner of 1.5 T was already introduced for clinical use in the 1980s and in 2002, General Electric, Philips and Siemens started the production of commercial scanners with a field strength of 3T. Currently, scanners with a magnet strength of 7T are used in clinical practices. They can image structures smaller than 1mm in the body. Research stretches this even further with experiments using magnets of more than 10T [26]. The image quality of an MRI scan is directly correlated with its Signal-to-Noise Ratio (SNR). Due to the increased power, the signal becomes stronger and thus, the SNR increases. This boosts the image quality in high field scanners.

While MRI can be used for imaging a variety of things, in this thesis, the focus will be on the medical aspect and thus on imaging the human body.

1.2. Low-field Imaging

In an effort to reduce the costs of an MRI scanner, research has been done in the field of low-field scanners. These types of scanners have a magnetic strength of less than 1.5T. While these scanners are of the same field strength as the first MRI scanners, current technology has enabled better hardware and software for imaging and processing. The construction of a cheaper MRI can be achieved by replacing the superconducting solenoid magnet with a different magnet, such as neodymium magnets in a Halbach formation or a neodymium dipole design [22]. By replacing the costly magnets with cheaper alternatives, the price of the scanners is significantly reduced. However, the use of cheaper magnets comes with a disadvantage: the magnetic field inside the scanner becomes non-linear, and the SNR decreases, which results in lower image quality. One of the main struggles in developing low-field scanners is finding the balance between decreasing the field strength and maintaining an image with an SNR that is high enough for clinical diagnosis. Reducing the size of the MRI makes it easier to transport them. Therefore, research into smaller and even as small as handheld MRI scanners is done. Various scanners of this type have shown promising results. This project focuses on image reconstruction for a handheld low-field MRI scanner developed by the LUMC and the TU Delft.

1.3. Artificial Intelligence in Medical Imaging

Artificial intelligence (AI) in medical imaging has been gaining momentum. AI techniques have been actively investigated in medical imaging. Their potential applications include image analysis and understanding, data acquisition and image reconstruction. AI uses algorithms to understand, dissect and predict on complicated data. The abundance of data available in the medical imaging field and the availability of computational power allow for training on various tasks. Each type of task has a specialised network or configuration. Various models have been able to reconstruct images from conventional MRI data, and even in low-field MRI, research has been done on image reconstruction via AI [21] [33] [15].

1.4. Research Contributions and Outline

This report will examine the following research question; Can deep learning-based image reconstruction improve image reconstruction for a low-field handheld MRI scanner?

This research question can be divided into two parts. First, do the signals of one measurement contain the information needed for image reconstruction? For this, correlations between simulated data and the measurement are investigated. Secondly, can image reconstruction for a low-field handheld scanner be improved via deep learning? Signals of simulated data will then be used as input for a deep learning model to see if image reconstruction can be improved for real data.

Therefore, the contributions of this research can also be divided into two sections. Firstly, investigating if the signals contain information needed for image reconstruction contributes to the potential of the handheld scanner. It contributes to the belief that this scanner can scan accurately and reproduce recognisable images. Secondly, deep learning-based image reconstruction investigates a different method of image reconstruction than used currently.

First, the background information needed for this project will be discussed. The experimental methods will then be elaborated on, the results will be shown and discussed, and finally, the research questions will be answered.

2

Background on MRI and Deep Learning

In this chapter, background information on MRI and deep learning are given. First, the physics of MRI are discussed in Section 2.1 after which conventional MRI is discussed in Section 2.2. Section 2.3 discusses the physical- and signal model of conventional image reconstruction, and Section 1.2 in low-field MRI is introduced. Section 2.5 focuses on handheld MRI, and finally, Section 2.6 discusses deep learning in medical imaging.

2.1. Physics of MRI

2.1.1. Nuclear spin resonance

Note: *In quantum mechanics, the nuclei of the ^1H cannot be described as a sphere. However, the classical model to describe nuclei is used for magnetic resonance.*

Imaging technology of the MRI is based on the property of subatomic particles known as *spin*. Not all particles exhibit spin; only in particles consisting of an uneven number of protons and neutrons spin can be found. Due to the composition of the body, the hydrogen nucleus (^1H) is mainly used in MRI, for it consists of a single proton and thus exhibits spin. Considering the nucleus of this hydrogen atom as a spin top, as shown in figure 2.1 left, its spin can be seen as a small magnetic axis through the nucleus. If a uniform magnetic field (B_0) is applied to these molecules, the axes align either parallel or anti-parallel (in the opposite direction) to the magnetic field. The portion of nuclei in the body that will proceed to be directed to the magnetic field is proportional to the magnetic field strength. The number of magnetised nuclei can be added together to become the Net Magnetic Vector (NMV). It is commonly accepted that about 60% of the human body consists of water, with two hydrogen atoms per molecule. The expectation would be that the NMV would be large. However, only 1 in 100 000 protons contribute to the signal at 1.5 Tesla [30]. Due to the aligning of the protons parallel and anti-parallel to

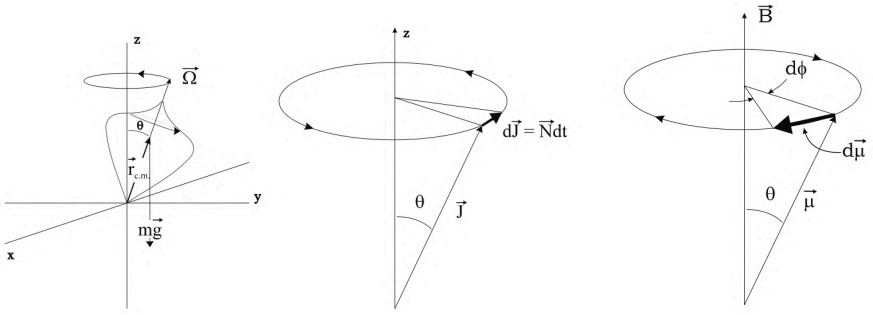

Figure 2.1: **Left** - A spinning top with an angular velocity Ω and a mass m precessing in an constant gravitational field. This field is positioned around the z-axis. **Centre** - The angular momentum diagram for a spinning top in a gravitational field showing how the torque leads to precession. **Right** - Visualisation of the precession in an magnetic field. Notice it is opposite to the direction of precession due to gravitational field. This is due to the fact that the gravitational field is directed the opposite direction as the magnetic field. As shown, the differential dφ is negative. Image retrieved from [6]

the magnetic field, the negative signal from the anti-parallel orientation and the positive signal from the parallel orientation cancel each other out. However, slightly more protons become aligned parallel with the magnetic field resulting in the Net Magnetic Vector.

Spin gives the nuclei another property that is important for MRI. Nuclei spin in an orientation with the axis of the nuclei at an angle to the magnetic field, similar to a spinning top laid on its side. This orientation results in a circular movement around the magnetic field orientation called the precession. The Lamor frequency can describe the frequency of this precession

$$f_L = \frac{\gamma}{2\pi} B, \tag{2.1}$$

in which $\gamma/2\pi$ is the gyromagnetic ratio in Hz/T that describes the ratio of its magnetic moment to its angular momentum, and B is the strength of the magnetic field in Tesla. The Larmor frequency is visualised in figure 2.1 on the right. Since the precession frequencies of the nuclei are in the range of electromagnetic waves, it is possible to excite the nuclei by sending a radio frequency pulse with the same frequency as the Larmor frequency. The result of this excitation is the flipping of the axis of the nuclei. The angle of flipping is dependent on the strength of the pulse and the duration of the pulse. When visualising the spinning top from Figure 2.1, the axis of the top will be flipped from the z-axis to the y axis and precess back to the z-axis via a movement similar to the path in Figure 2.2. Typically an excitation pulse of 90 degrees is used. After excitation, the nuclei slowly fall back to their equilibrium state while emitting energy in the form of electromagnetic radiation. This radiation has a wavelength proportional to the Larmor frequency of the excited proton.

After the 90 degrees excitation pulse, all rotation axes of the nuclei will spin with a precession perpendicular to the magnetic field B_0. However, the precession will begin to spin out of phase. This is due to chemical differences between the different protons and the property used for imaging.

2.1.2. Signal Formation

The process of protons returning to their original state after excitation was first described by [1]. While the advances in technology have been significant since this publication, the theory is still the basis of MRI imaging. When assuming the Net Magnetic Vector (NMV) with a precession around an axis it can be split into three vectors with a cartesian direction and dependent on time: $M_x(t)$, $M_y(t)$ and $M_z(t)$ in which $M_x(t)$ and $M_y(t)$ are the transverse components, for they operate on the transverse plane, and $M_z(t)$ the longitudinal component. The process of net magnetisation M is governed by the Bloch equations and in the content of MRI has the following form:

$$\frac{dM}{dt} = \gamma M \times B_{ext} + \frac{1}{T1}(M_0 - M_z)\hat{z} - \frac{1}{T_2} M_\perp \tag{2.2}$$

In this T_1 and T_2 describe the return to equilibrium for a field pointing in the z-axis. T_1 describes the time it takes for the longitudinal magnetisation to increase to its equilibrium. T_2 describes the decrease in angular frequency ω after excitation. When solving the Bloch equation for a constant field B_{ext} = B_0 the cross product in Equation 2.2 results in the following three components

$$\frac{dM_x}{dt} = -\omega_0 M_y - \frac{M_x}{T_2} \tag{2.3}$$

$$\frac{dM_y}{dt} = \omega_0 M_y - \frac{M_y}{T_2} \tag{2.4}$$

$$\frac{dM_z}{dt} = \frac{M_0 - M_z}{T_1} \tag{2.5}$$

in which $\omega_0 \equiv \gamma B_0$.

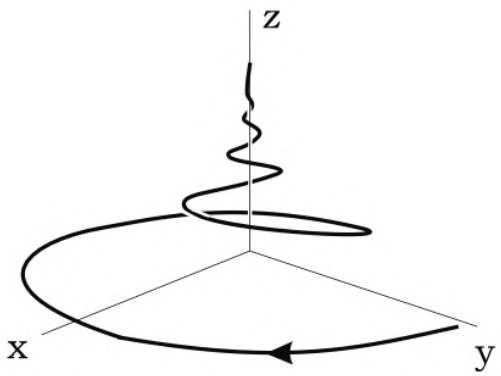

Figure 2.2: The path of the magnetisation vector shows the decay of transverse components and the regrowth of the longitudinal magnetisation. The reference frame is the laboratory, and the initial value was along the y-axis. It can be seen that both the regrowth and the decay components influence each other. Image retrieved from [6].

Intuitively, and when considering Figure 2.2, it can be seen that while $M_z(t)$ only has a direction, combining $M_x(t)$ and $M_y(t)$ results in a circular motion with an angular frequency $\omega_0 \equiv \gamma B_0$. $M_x(t)$, $M_y(t)$ and $M_z(t)$ should therefore be constructed of the form

$$M_x(t) = A * \sin(\omega * t) \tag{2.6}$$

$$M_y(t) = A * \cos(\omega * t) \tag{2.7}$$

$$M_z(t) = C \tag{2.8}$$

in which ω is the angular frequency, t is the time, A a scaling factor and C a constant dependent on the time t. These formulas, however, do not explain the process of the protons returning to their original state after excitation. Incorporating T_1 and T_2 into the vectors of Equations 2.6, 2.7 and 2.8 and evaluating Equations 2.3, 2.4 and 2.5 with $M_x = m_x e^{-t/T_2}$ and $M_y = m_y e^{-t/T_2}$ (the integrating factors) the following set of solutions can be found:

$$M_x(t) = \exp^{-t/T_2}\left(M_x(0)\cos(\omega_0 t) + M_y(0)\sin(\omega_0 t)\right) \tag{2.9}$$

$$M_y(t) = \exp^{-t/T_2}\left(M_y(0)\cos(\omega_0 t) + M_x(0)\sin(\omega_0 t)\right) \tag{2.10}$$

$$M_z(t) = M_z(0)\exp^{-t/T_1} + M_0\left(1 - \exp^{-t/T_1}\right) \tag{2.11}$$

in which M_0 represents the magnetisation before excitation in Tesla (T), t is the time in ms, T_1 and T_2 are also measured in ms, and ω_0 is the angular frequency. For a more thorough background on the physics behind MRI see [6].

Figure 2.3 shows the regrowth of the longitudinal component of the magnetisation from the initial value $M_z(0)$ to the equilibrium value M_0 governed by T_1 on the left. It can be seen that that T_1 is the time it takes $M_z(0)$ to reach (1 − 1/e) or about 63% of its maximum value (M_0). On the right, it shows the decay of the magnitude of the transverse magnetisation from an initial value governed by T_2. It can be seen that T_2 is the time required for the transverse magnetisation to decrease to 1/e or 37% of its original value.

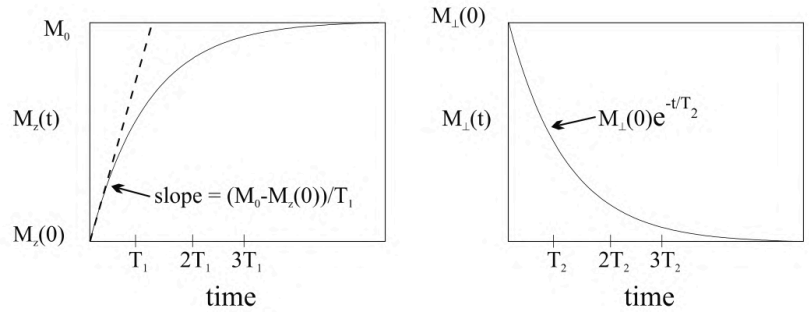

Figure 2.3: **Left** - the regrowth of the longitudinal component of the magnetisation from the initial value $M_z(0)$ to the equilibrium value M_0 governed by T_1. **Right** - The decay of the magnitude of the transverse magnetisation from an initial value governed by T_2. Image retrieved from [6]

Tissue	ρ (%)	T_1 (ms)	T_2 (ms)
white matter	72	500	90
grey matter	83	600	100
brain fluid	100	2000	1000
liver	65	500	40
oxidised blood	100	1500	50
deoxidised blood	100	1500	200
fat	60	200	80
bone	25	>10^2	<1

Table 2.1: Hydrogen density in percentage (compared to water) and approximate T_1 and T_2 relaxation times for different tissues at 1.5T. It can be seen that the T1 is always higher than the T2 for a specific tissue. [27]

While T_2 describes the decrease in angular frequency ω after excitation, decay in NMR experiments is faster than would be predicted by atomic and molecular mechanisms. The observed decay is therefore not the pure T_2 but is denoted as T_2^* and consists of the true T_2 and the effects of the inhomogeneities of the main magnetic field [9] as shown below:

$$\frac{1}{T_2^*} = \frac{1}{T_2} + \frac{1}{T_{2i}} \tag{2.12}$$

in which T_{2i} describes the effect the inhomogeneities of the main magnetic field have on the observed decay [9]. With this knowledge T_2 in Equation 2.10 and 2.9 should be replaced with T_2^*.

When visualising T_1 and T_2 in a spinning top such as the one represented in Figure 2.1 it can be seen that there is a correlation between T_1 and T_2. Figure 2.2 shows this property even clearer: When a proton relaxes towards the net magnetisation (T_1 relaxation) there will be dephasing resulting in T_2 relaxation. Due to their physical composition, different tissues have different relaxation times T_1 and T_2, as can be seen in Table 2.1. This effect allows for differentiation between different tissues when scanning by varying the imaging time. This creates images that are either T_1 weighted or T_2 weighted. It can also be seen in Table 2.1 that T_1 of a specific tissue type is always higher than its T_2. Note that this Table is an approximation of T_1 and T_2 relaxation times for 1,5T, and not precise values, for variations in relaxation times are so great that it is a research field in itself [3].

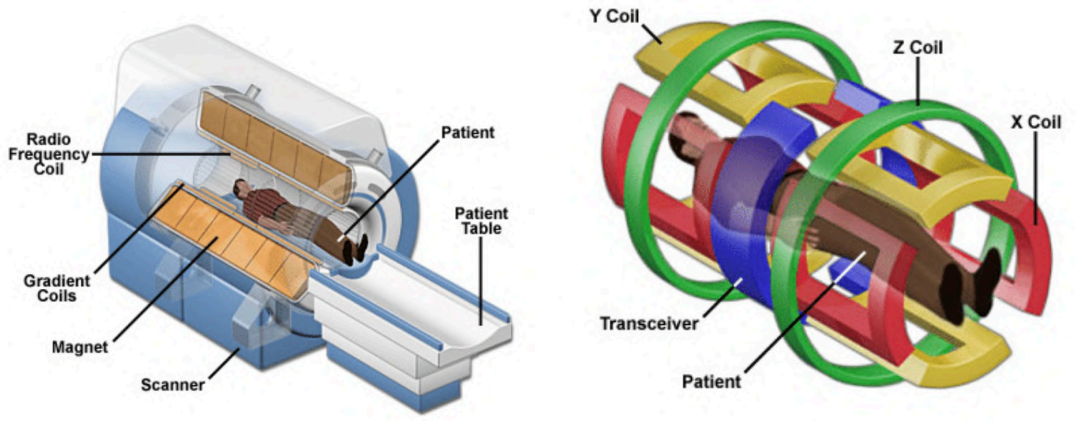

Figure 2.4: MRI scanner and its gradient coils. **Left** - MRI scanner with a patient in it. **Right** - The gradient coils and the transceiver visualised around the patient. Images retrieved from [11].

2.2. Conventional MRI

2.2.1. Hardware

The main component of an MRI is its main magnet which can generally be divided into two different types of magnets, open bore or closed bore. Closed bore magnets typically consist of cylindrical superconducting magnets of multiple solenoidal coils. These superconducting magnets can achieve high magnetic field strengths, for the wire surrounding the magnet does not have an electrical resistance when cooled to cryogenic temperatures. In theory, these magnets would produce a homogeneous field if the magnet was infinitely long. However, an MRI scanner is only 2-3 meters long and to achieve a homogeneous magnetic field inside such a scanner, the solenoidal coils are split into smaller cylinders, resulting in a configuration that approaches homogeneity in the scanner. This configuration often consists of 6-10 magnets. Besides improving the homogeneity in the magnet's centre, it reduces fringe fields at the ends of the scanner.

Inside this main magnet, the gradient coils can be found. These gradient coils apply a variation in the homogeneous field. They can be used in image reconstruction to identify where the signal originated. The gradient coils in the X and Y direction consist of a saddle-like structure, visualised in Figure 2.4, while the Z-coil consists of a circular coil around the patient.

Another essential component positioned inside the MRI scanner is the Radio Frequency-coil (RF-coil) which can be receiving, transmitting or both. When the coil is transmitting, it generates the B_1 field that is perpendicular to the B_0 field. This B_1 is only turned on for milliseconds in which it induces the radio frequency pulse (RF-pulse). When the RF-coil is receiving it is responsible for detecting the signal emitted by the excited protons in the scanned object/body.

2.2.2. Image Acquisition

In Section 2.1.2 the difference between T_1, T_2 and T_2^* has been discussed. While it has been explained that different relaxation times result in different types of images, it does not paint the whole picture, for there are two other variables that have a great influence on the image: the repetition time (T_r) and the echo time (T_E). These two variables govern the amount of relaxation before the next pulse occurs, e.g. how much the image is T_1 or T_2 weighted. T_r describes the time in between two or more RF pulses, and T_E describes the time before an echo occurs.

Type of MR signal	Method of Formation	MR Signal
Free induction decay (FID)	1 RF pulse	Oscillating at Larmor Freq governed by T_2^*
Spin Echo (SE)	2 RF pulses	Initial pulse and an echo pulse at $t = 2t$
Stimulated Echo	3 or more RF pulses	Initial pulse and multiple echo pulses

Table 2.2: Overview of different types of MR signals and their method of formation.

2.3. Conventional Image Reconstruction

The signal $S(t)$ that the receiving RF-coil receives consists of a value for each voxel (volume pixel). This data is saved in a so-called k-space, an array of numbers representing the spatial frequencies in the MR image. Receiving and saving the data in k-space enables faster imaging, for calculations in the frequency domain are less costly, and the use of Fourier Transforms (FT) can then reconstruct the image.

The image reconstruction elaborated on this section is based on the image reconstruction as discussed in [13].

2.3.1. Physical model

While (2.9), (2.10) and (2.11) are formulated to understand the difference between T_2 and T_1 weighting, to be able to correctly visualise the signal model it is better to start back at the original net magnetisation which is proportional to the B_0 field and the time (t) that the magnetic field is applied.

$$\vec{M}(\vec{r},t) = M_x(\vec{r},t)\vec{i} + M_y(\vec{r},t)\vec{j} + M_z(\vec{r},t)\vec{k} \tag{2.13}$$

The Larmor frequency (Equation 2.1) can also be described as a function of $B_z(\vec{r},t)$ and then describes the instantaneous frequency at a given spatial location.

$$\omega(\vec{r},t) = \gamma B_z(\vec{r},t). \tag{2.14}$$

Due to the excitation, explained in Chapter 2.1, the net magnetisation of Equation 2.13 is tipped into the transverse plane and can be described as a complex function as it consists of two vectors.

$$M(\vec{r},t) \triangleq M_x(\vec{r},t) + iM_y(\vec{r},t) \tag{2.15}$$

Due to the complex properties of the precession frequency and the magnetisation in the transverse plane, these can be combined to describe the behaviour after the excitation pulse. If $t = 0$ is when the excitation pulse is complete, then at a certain time point $t > 0$, the readout occurs. The precession of the net magnetisation in the transverse plane can then be described as an integral of the instantaneous frequency in Equation 2.14 [13].

$$M(\vec{r},t) = M(\vec{r},0)exp\left(-i\int_0^t \omega(\vec{r},t')dt'\right) \tag{2.16}$$

Equation 2.16 describes the ideal situation, for it does not account for any variations in the field. In practice, however, these variations are present and influence the field. To be precise, the spins can become out of phase within a given voxel due to microscopic variations in the field strength. This property is described by T_2^* and when accounting for this decay, Equation 2.16 becomes

$$M(\vec{r},t) = f(\vec{r})e^{-t/T_2^*(\vec{r})}exp\left(-i\int_0^t \omega(\vec{r},t')dt'\right) \tag{2.17}$$

in which $f(\vec{r}) \triangleq \vec{M}(\vec{r},0)$ represents the transverse magnetisation directly after the excitation. This notation can only be used when the scanned object is static so $f(\vec{r})$ is not a function of time.

2.3.2. Signal Model

The signal acquired in a conventional high field MRI after excitation is discussed in this section.

According to Faraday's law, electrical potential $v(t)$ across a receiver coil is

$$v(t) = \int c(\vec{r})\frac{d}{dt}M(\vec{r},t)d\vec{r} \tag{2.18}$$

in which M represents the time-varying magnetisation in a nearby coil and $c(\vec{r})$ the coil response pattern which decreases with the distance from the coil. A narrow-band approximation is often used for the time constant of T_2^* is in the order of milliseconds while the phase variations in Equation 2.17 are in the

order of MHz. This allows for the approximation of $d/dtM(\vec{r},t) \approx c_0 M(\vec{r},t)$ and Equation 2.18 can be rewritten as

$$v(t) = \int c(\vec{r}) M(\vec{r},t) d\vec{r}. \tag{2.19}$$

The signal is amplified and demodulated, often with quadrature demodulation resulting in two separate signals, in-phase $I(t)$ and quadrature $Q(t)$ baseband signal.

$$s(t) \triangleq I(t) + iQ(t) = lowpass(e^{i\omega_0 t} v(t)) = e^{-i\omega_0} \int c(\vec{r}) M(\vec{r},t) d(\vec{r}) \tag{2.20}$$

The lowpass filter selects the baseband component of the demodulated signal. While the imaginary representation suggests otherwise, both the $I(t)$ and $Q(t)$ are sampled and digitalised, resulting in two different signals.

If $c_l(\vec{r})$ denotes the sensitivity of lth coil for l = 1, ... L with L number of coils. $s(t)$ refers to the 'MR Signal' for the lth coil as shown in Equation 2.20. When combining the MR Signal with the transverse magnetisation directly after excitation, as defined in Equation 2.17, after simplifying a general forward model can be constructed,

$$s_l = \int c_l(\vec{r}) f(\vec{r}) e^{-t/T_2^*(\vec{r})} e^{-i\phi(\vec{r},t)} d(\vec{r}) \tag{2.21}$$

in which the time- and space-varying phase is

$$\phi(\vec{r},t) \triangleq \int_0^t (\gamma B_z(\vec{r},t') - \omega_0) dt'. \tag{2.22}$$

The signal received by the MRI consists of noisy samples of the signal model described in Equation 2.21,

$$y_{li} = s_l(t_i) + \varepsilon_{li}, \quad i = 1, \dots, n_d, \quad l = 1, \dots, L, \tag{2.23}$$

in which y_{li} refers to the ith sample of the lth coil's signal at time t_i, n_d refers to the amount of time samples and ε_{li} the measurements errors.

2.3.3. Reconstruction

Reconstruction of the image can be done when combining the measurement model from (2.23) and the signal model from (2.21) to estimate $f(\vec{r})$ from the measurement vector $\mathbf{y} = (\mathbf{y}_1, \dots, \mathbf{y}_L)$ where $\mathbf{y}_l = (y_{l1}, \dots, y_{l,n_d})$. When insufficient samples are taken, this linear approach results in an ill-posed problem for the measurements of y are discrete while $f(\vec{r})$ is an continuous function. To be able to do a parametric estimation, $f(\vec{r})$ can be approximated as a finite series expansion,

$$f(\vec{r}) = \sum_{j=1}^{N} f_j b(\vec{r} - \vec{r}_j), \tag{2.24}$$

in which $b(\cdot)$ represents the object basis function, $\vec{r}_j$ the center of the jth translation of the basis function and with N indicating the amount of parameters. While the true parametric model can never be satisfied, simple basis functions can be used to approximate this ([14]). An approximation with rectangular basis functions can be used. $b(\vec{r}) = \text{rect}\,(\vec{r}/\Delta)$ to represent the cubic voxels or square pixels or and with N representing the amount of voxels or pixels.

The combination and simplification of Equation 2.21 and the series expansion in Equation 2.24 result in the discrete forward model

$$s_l(t_i) = \sum_{j=1}^{N} a_{lij} f_j. \tag{2.25}$$

in which an assumption is made that A_{ij} is highly local so 'centre voxel' approximation can be made in the form of

$$a_{lij} \approx c_l(\vec{r}_j) e^{-t_i/T_2^*(\vec{r}_j)} e^{-\iota\phi(\vec{r}_j,t_i)} \tag{2.26}$$

Representing the combination of the measurement model in Equation 2.23 and the discrete forward model in Equation 2.25 in matrix-vector form results in

$$y_l = \mathbf{A}_l \mathbf{f} + \varepsilon_l, \tag{2.27}$$

in which the pixel values are represented by $\mathbf{f}$. As the goal in conventional high field MRI is to combine all L coils as $\mathbf{y} = (\mathbf{y}_1, \ldots, \mathbf{y}_L)$ the system matrix is defined as $\mathbf{A} = (\mathbf{A}_1, \ldots, \mathbf{A}_L)$ to result in the linear model

$$y = \mathbf{A}\mathbf{f} + \varepsilon. \tag{2.28}$$

While this representation seems simple to solve, problems arise when considering that the elements of $\mathbf{A}$ result in an $\mathbf{A}$ that is too large to store.

2.4. Low-field MRI

As mentioned previously in section 1.2, there can be great value for low-field MRI scanners. Costs of scanners can be brought down due to changes in the hardware; While these changes in the hardware result in a poorer signal-to-noise ratio (SNR) than high-field scanners, they result in smaller, more robust scanners.

2.4.1. Hardware

While superconductor magnets are often used in high field MRI due to their ability to reach high field strengths, this is something that is not necessary for low-field MRI. In these low-field scanners, permanent magnets create the magnetic field. By placing multiple magnets in a specific orientation, aperture fields can be increased on one side as they decrease on the other, as shown by [17]. For low-field scanners in the order of 0.25-0.5T, these often are categorised in two groups, the first having a permanent magnet based on neodymium-iron-boron and the second with an additional electromagnet. These permanent magnets are either shaped in a C with a single ferromagnetic yoke or can consist of two separate ferromagnetic yokes and are shaped like an H [22].

The magnetic field produced by these permanent magnets can be calculated via the vector potential (A) at point x

$$\vec{A}(\vec{x}) = \frac{\mu_0}{4\pi} \oint \frac{\vec{M}(\vec{x}') \times \vec{n}'}{|\vec{x} - \vec{x}'|} da' \tag{2.29}$$

with M as the volume of the magnetisation of the magnet, n the normal vector to the surface at point x' and μ_0 the permeability of vacuum with the integral evaluated over the entire surface of the magnet.

The gradients' design typically differs from those used in scanners with cylindrical bore magnets. Open MRI systems use planar coils referred to as bi-planar gradient coils. These planar gradients consist of wire patterns that produce the gradients and are positioned at each opposing magnetic pole. As in cylindrical scanners, the x- and y-configuration are of similar shape with a 90 degrees difference in orientation. With the configuration of the gradients as such, the open space in between the two opposing poles is maximised [23].

2.4.2. Scanner TU Delft/LUMC

Previous projects have used scanners constructed by the Leids Universitair Medisch Centrum (LUMC) and TU Delft. One of these scanners is discussed in this section for insights found in projects on this low-field scanner are used in the handheld MRI project. The scanner used in previous graduation projects such as [15] and [7] has been designed for imaging of the head and consists of four permanent circular Halbach arrays stacked together to create the fairly homogeneous B_0. Extra magnet rings are placed to minimise inhomogeneities in the z-direction and create linear variations in the magnetic field in x- and y-direction. The field strength then varies from about 0.55 mT to 0.59 mT. Due to this linear variation of the magnetic field, gradients are not needed as the variation can directly be used for image reconstruction, as explained in the next section. A more detailed description of this prototype and the magnets can be found in [4].

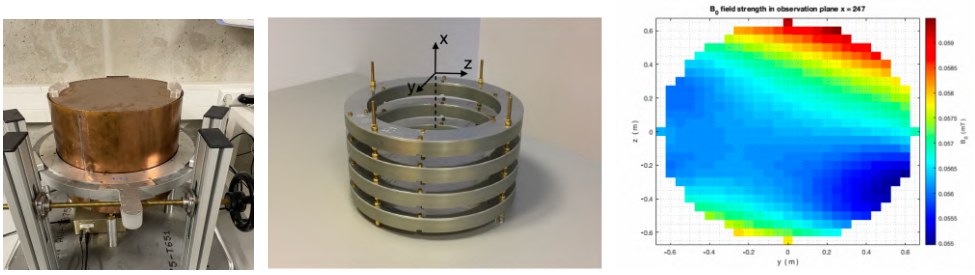

Figure 2.5: **Left** - The low-field scanner from the TU Delft and LUMC. **Centre** - The Halbach magnet rings of the low-field scanner. It can be seen that there are multiple stacked on top of each other. **Right** - The constant B_0 field inside the low-field scanner. Centre and right image retrieved from [15].

The low-field scanner constructed by the LUMC and TU Delft creates a relatively homogeneous B_1-field after sending out the RF pulses. However, due to the absence of gradient coils, spacial encoding for conventional two-dimensional image reconstruction as in Section 2.3.3 cannot be used as they rely on high strength linear spatial encoding magnetic fields (SEMs) and a homogeneous B_0-field. However, two-dimensional imaging has been performed without gradient coils in a low-field scanner. Based on literature [10], the inhomogeneity of B_0 can be used for spatial encoding by rotating the magnet around the object. The inhomogeneous field pattern can be used as a rotating spatial encoding magnetic fields (rSEMs). This approach creates projections from different angles from which the two-dimensional image can be reconstructed and has been used in research with the low-field scanner of the TU Delft/LUMC [15]. This technique is performed in scanners that can rotate around the scanned object and is thus applicable in conventional MRIs. Section 2.5.1 discusses how this application can be used in a handheld scanner. Due to the inhomogeneous magnetic field in low-field MRI, a standard inverse Fourier transform cannot be performed to reconstruct the image and this results in Equation 2.28 to be ill-posed. To be able to reconstruct the image, model-based reconstruction, as proposed by [5], can be done. This method uses a regularisation penalty for the least-squares minimisation problem to evaluate the ill-posed reconstruction problem of Equation 2.28. This results in two different reconstructed images for each scan, one solved with the use of the conjugate least-squares minimisation problem (CGLS) and solved with the use of generalised conjugate gradient minimal error (GCGME). For this project, this image reconstruction algorithm for low-field MRI proposed by [5] is considered.

2.5. Handheld MRI

When low-field scanners improved, the idea of a smaller, single-sided scanner was explored by different research groups. The NMR-MObile Universal Surface Explorer (MOUSE), a scanner with two permanent magnets that generated a static magnetic field, was presented by [2]. Using a solenoidal RF coil in the gap between the two magnets ensured that the static polarising magnetic field B_0 and the RF field B_1 were approximately orthogonal to each other. The principle of the NRM MOUSE has since then been explored by various researchers for different purposes, from medical purposes such as brain imaging with a cap-shaped single-sided scanner [24], assessing burn depth in skin [18] to 3D imaging of depth profiles [29], [8], [16].

2.5.1. Scanner TU Delft/LUMC

A handheld scanner has also been constructed in the LUMC in collaboration with the TU Delft. The main components of the scanner are a permanent magnet and a RF coil. The permanent magnet consists of multiple permanent magnets fixed in a 3D printed casing, which can be seen in Figure 2.9 on the top right. The magnets combined create the main magnetic field B_0 that has a gradient perpendicular to the surface of the magnet, as can be seen in Figure 2.7. The coil of this scanner is wrapped around the sample and has a diameter of 15mm. The top of the sample can be seen in Figure 2.9 in the bottom image. The magnet and the coil are positioned inside the isolated casing. The coil can be seen in Figure 2.9 on the right, wrapped around the sample, and the magnet can be seen in Figure 2.6 on the top right inside the casing. Since this scanner does not move around the sample, rSEMs, which are explained in Section 2.3, can not be used to reconstruct images. For this reason, translations are

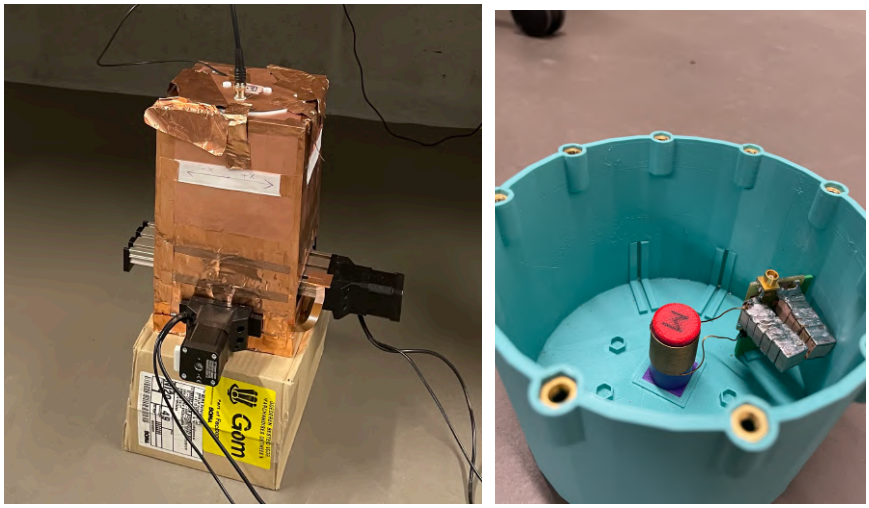

Figure 2.6: **Left**: The handheld scanner constructed by the LUMC and TU Delft. The casing is isolated and the runners can be seen at the bottom. **Right**: The inside of the scanner. The coil can be seen wrapped around the sample.

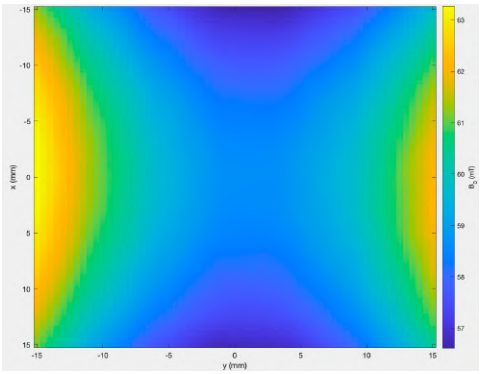

Figure 2.7: The gradient of the magnetic field B_0 produced by the handheld scanner. Retrieved from [28]

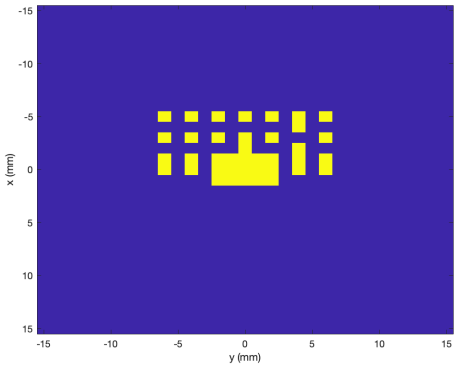

Figure 2.8: Translations used for measurements. Each yellow square represents one measurement location. A total of 39 translations are visualised here.

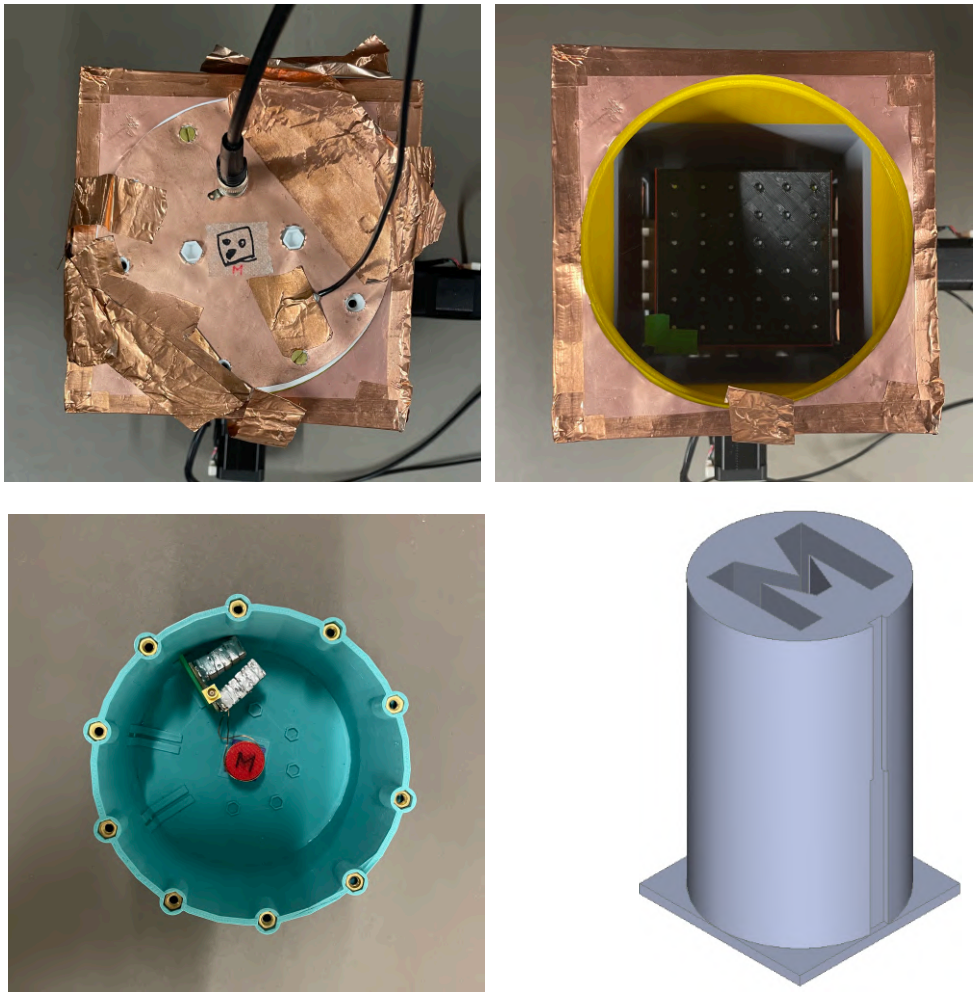

Figure 2.9: **Left top** - The handheld scanner viewed from the top. **Right top** - The inside of the handheld scanner. The magnets are positioned inside the black box. **Left bottom** - The coil and sample inside the scanner. The coil is wrapped around the red M. The blue container fits inside the scanner. **Right bottom** - A schematic of the phantom inside the scanner in which the cut out of the M can be seen.

implemented. These translations consist of the magnet being replaced in different positions under the coil. The translations ensure that the sample is at a different location in the magnetic field in each measurement and results in a similar reconstruction model as with rSEMs. The translations are carried out by two runners, one in the x-direction and one in the y-direction, and can be seen in Figure 2.6 and Figure 2.9 on the top images. Due to the non-linear field, the translations give more information with each move.

2.5.2. Data

Measurements with this scanner have been done at the LUMC. The M that can be seen in Figure 2.6 on the right image with the coil wrapped around it was the phantom in these measurements and consists of a plastic 3D printed cylinder with an M-shaped cutout with a depth of half the cylinder. This cutout is filled with a few drops of sunflower oil. A schematic of the phantom can be seen in Figure 2.9 on the bottom right. In the measurements, 39 translations were performed, the orientation of which can be seen in Figure 2.8 in which a repetition time of 200 ms, an echo time of 20 ms and a dwell time of 5 µs was used. Each measurement consists of 512 data points and 2000 averages for each translation. Model-based image reconstruction, as proposed by [5], resulted in a reconstruction in which the contours of the scanned M were visible, which can be seen in Figure 2.10.

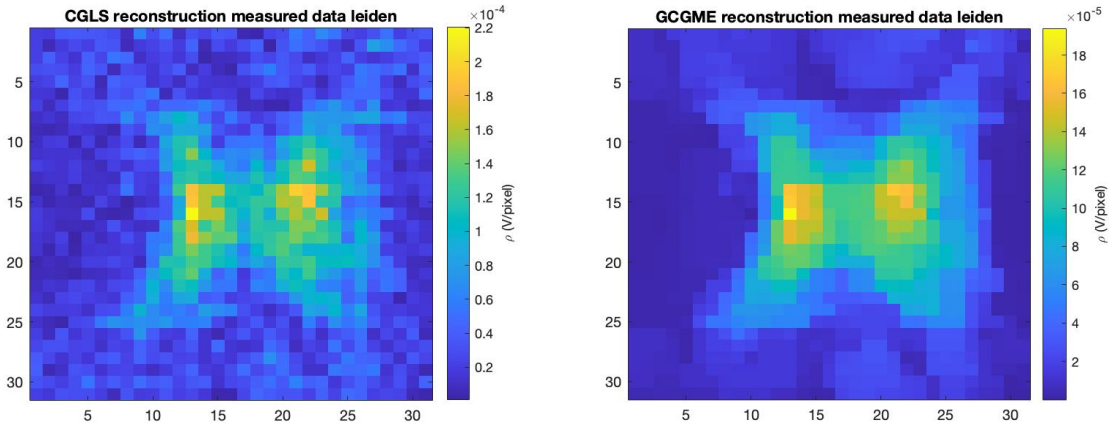

Figure 2.10: Image after model-based image reconstruction. On the left reconstruction is done by solving the ill posed problem with conjugate gradient least squares (CGLS) and on the right with generalised conjugate gradient minimal error (GCGME)

2.6. Deep learning

Artificial intelligence in a medical context has seen exponential growth in recent years. A subsection of this field, deep learning (DL), has become widely used in research due to its high generalisation capacity and its high performance. Combining this with a large amount of medical data and the powerful computers available results in opportunities in medical image reconstruction, segmentation and enhancement tasks.

In deep learning, the aim is to be able to make decisions by recognising the desired output based on a given input. Loosely mimicked by the neuron structure in the brain, multiple neurons are connected in a deep learning model in which the connections are weighted to classify the characteristics on which to categorise. During training, the associations between the input and the desired output are actively weighted and evaluated through a loss function. This loss function indicates the quality of the predictions compared to the expected outcome. This loss function is iteratively reduced by tweaking the weights between the neurons for the next training batch. For image-based problems, this is often done on a pixel-wise basis.

Deep learning is widely used in medical imaging because of the availability of images to train on, for one of the problems in deep learning is the abundance of data to train on. To iteratively reduce the loss function, there has to be enough data available to train multiple times without overfitting. In overfitting, the model predicts to closely to one specific data set and may fail to fit or predict on new data. Underfitting is the opposite and will happen when the model is not complex enough to understand the data. This will occur, for instance, when fitting a linear model to non-linear data. With a reduction of the loss function, one can assume the model is moving from underfitting, and by checking the model with unseen data after each iteration, overfitting can be avoided.

2.6.1. Model

In medical image-based deep learning, different models are used for different tasks. UNet's are commonly used for tasks in which the input and the output are both images, such as segmentation tasks [32]. At the same time, models such as ResNet's are used for classification tasks by linking fully connected layers with different classifiers [31]. Research has shown promising results for model-based image reconstruction for low-field MRI signals with automated transform by manifold approximation (AUTOMAP) [15]. AUTOMAP is a neural network used for image reconstruction of conventional k-space MRI data. It consists of two fully connected layers followed by two hidden layers, both activated by the hyperbolic tangent function, two convolutionals layers followed by rectifier nonlinearity and a final deconvolutional layer. For a more detailed description, see [34].

3

Methods

In this chapter, the approach used in this project is described. Initially, the data used in this project is discussed, the acquisition (Section 3.1.1) and the method of inspection (Section 3.1.2). Section 3.2.1 describes the model architecture used for deep learning, and Section 3.2.2 describes the data, and its augmentations, used.

3.1. Data

3.1.1. Data Acquisition

The data collected in the LUMC and described in Section 2.5.2 and shown in Figure 2.10 consists of measurements from which we know that the shape of an M was measured. While the image reconstruction shows an image in which we vaguely can see the contours of an M, it is interesting to see if the reconstruction and the received signal have a greater correlation with a simulation of the letter M than with other letters of the alphabet. For this reason, a simulation data set consisting of all the letters in the alphabet, capital and small, is constructed. These letters are visualised in Figure 3.1 and 3.2 and consists of 2 sets of 24 files of 64x64 pixels. The intensity of the background in each is 0, and the intensity of the letter itself is $2,2 * 10^{-4}$. The intensity of the letter has the same intensity as the highest intensity found in the measured data. All letters are situated in the centre of the file with a border of 15 pixels around them. It can be seen that the small letters in Figure 3.2 are smaller in size than the capital letters in 3.1, and they are positioned a bit lower in the image, just as letters in writing are. This ensures a difference between letters that have the same shape in capital and small letters, such as the small c and the capital C.

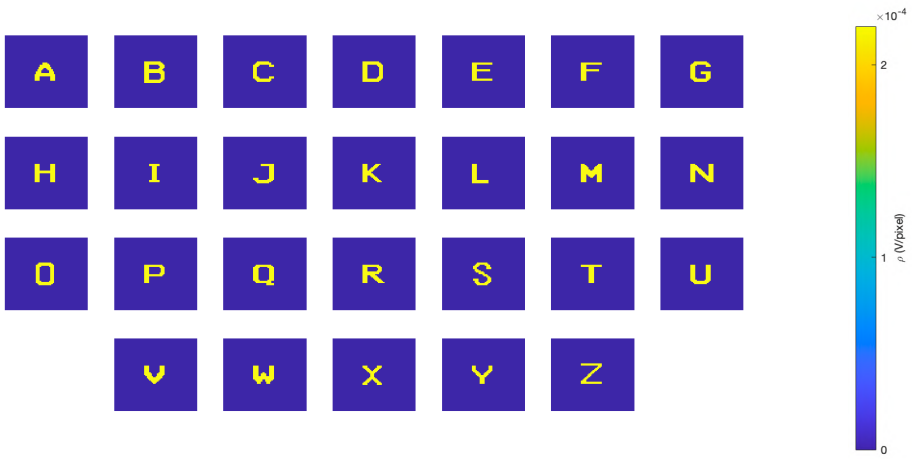

Figure 3.1: Data set of capital letters. Each letter has an intensity of $2,2 * 10^{-4}$ and an background of 0.

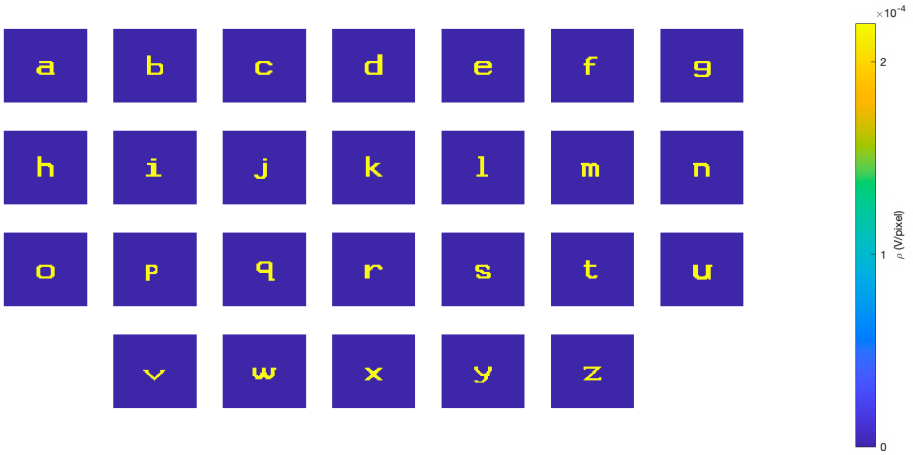

Figure 3.2: Data set of small letters. Each letter has an intensity of $2,2 * 10^{-4}$ and an background of 0.

3.1.2. Data Inspection

To investigate the correlation between the measurements conducted in the LUMC of the M and phantoms of all separate letters, the correlation between the reconstructed image and the simulations are calculated pixel-wise for each whole image. The correlation is found via

$$r = \frac{\sum_m \sum_n \left(A_{mn} - \overline{A}\right)\left(B_{mn} - \overline{B}\right)}{\sqrt{\left(\sum_m \sum_n \left(A_{mn} - \overline{A}\right)^2\right)\left(\sum_m \sum_n \left(B_{mn} - \overline{B}\right)^2\right)}} \tag{3.1}$$

in which A represents the measurement and B the phantom letter and $\overline{A}$ and $\overline{B}$ the mean intensity of each image. Figure 2.10 is used as input for the measurements and correlated with the phantom letters (seen in Figure 3.1 and 3.2). For the measured data, both CGLS- and GCGME reconstruction are considered independently.

Section 2.3.3 describes the formation of Equation 2.28, which can be solved for image reconstruction. Equation 2.28 can be rewritten to

$$\mathbf{b} = \mathbf{Ax} \tag{3.2}$$

in which $\mathbf{b}$ is the signal measured at discrete time instances, $\mathbf{x}$ is the unknown image and $\mathbf{A}$ is the model matrix. When considering Equation 3.2 one should assume that a different $\mathbf{b}$ signal will result in a different image $\mathbf{x}$ with the same model matrix $\mathbf{A}$. Using the same $\mathbf{A}$ as for the measured data, a complex $\mathbf{b}$-vector of each letter is constructed. The correlation between these simulated vectors for each separate small and capital letter and the measured vector is found via

$$\hat{R}_{xy}(m) = \begin{cases} \sum_{n=0}^{N-M-1} x_{n+m} y_n & m \geq 0 \\ -\hat{R}_{yx}(-m) & m < 0 \end{cases} \tag{3.3}$$

in which R is the correlation for each signal, x and y are input vectors with length N. This results in an output vector in which the highest value represents the maximum correlation. The correlation is normalised so the autocorrelations at zero lag are identically 1.0.

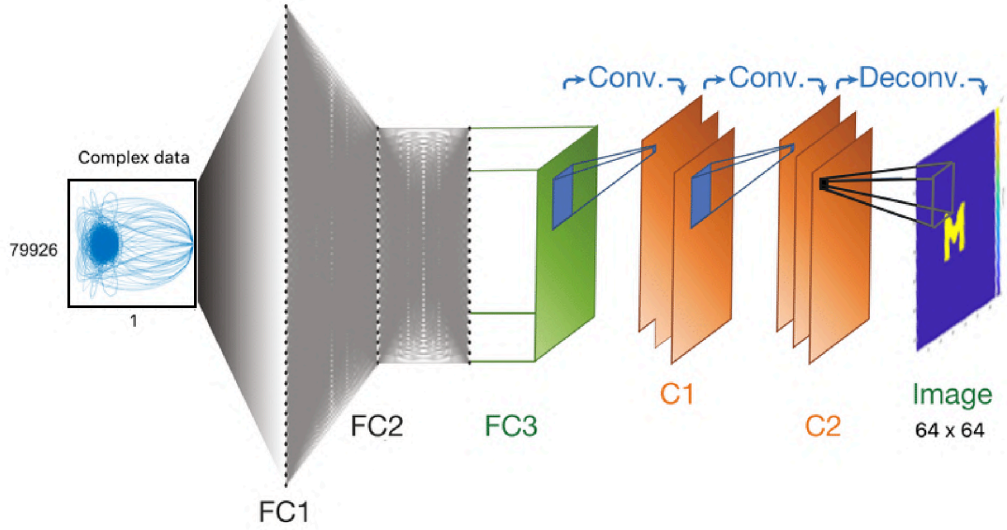

Figure 3.3: The AUTOMAP Network visualised. The input data in .the form of 79926x1 can be seen on the left. It is connected to two fully connected layers. In the first layer, the data is enlarged to $(79926x1)^2$ after which it is down-scaled again to $79926x1$. The final hidden layer is reshaped to a 64x64 matrix for convolutional processing. This is followed by two convolutional layers and a deconvolutional layer. Finally, it results in a prediction of a 64x64 image.

To inspect if the reconstructed image is most likely to be a capital M instead of an other letter, the correlations, as described in this section, are added and normalised via

$$R_{total} = \frac{\frac{R_{cgls}+R_{GCGME}}{2} + R_{signal}}{2} \tag{3.4}$$

in which R_{CGLS} is the correlation found between the simulated image and the reconstruction via CGLS, R_{GCGME} the correlation found between the simulated image and the reconstruction via GCGME and R_{signal} the correlation between the simulated signal and the measured signal. Since there are two correlations for the reconstructed images and only one for the signal, these correlations are already normalised by adding them and dividing by 2. This ensures that the reconstructed image has the same influence on the total correlation R_{total} as the signal. By inspecting these correlations we aim to eliminate the coincidence that the measured M just looks like an M but aim to prove that it is in fact an M.

3.2. Deep learning

3.2.1. Architecture

For this experiment a network is constructed that is based on the AUTOMAP network discussed in Section 2.6. The AUTOMAP architecture uses k-space signals from a conventional MRI to reconstruct the images. While our data is not k-space, the process of using signals to predict the corresponding image is similar. The network used in this project is visualised in Figure 3.3. The input layer is fully connected to a hidden layer and is activated by a ReLu activation function. The final hidden layer is then reshaped to a 64x64 matrix for convolutional processing. Two convolution layers are used with a He kernel initializer, each with a filter f that convolves with stride 1 and is followed by a ReLu activation function. Finally, deconvolution with a Sigmoid activation function is performed, and the output shows the reconstructed image of 64x64. The mean squared error (MSE) is used to evaluate the model via

$$MSE = \frac{\sum(y_i - \hat{y}_i)^2}{n} \tag{3.5}$$

in which y_i is the ith observed value, $\hat{y}_i$ the corresponding predicted value and n the total number of observations.

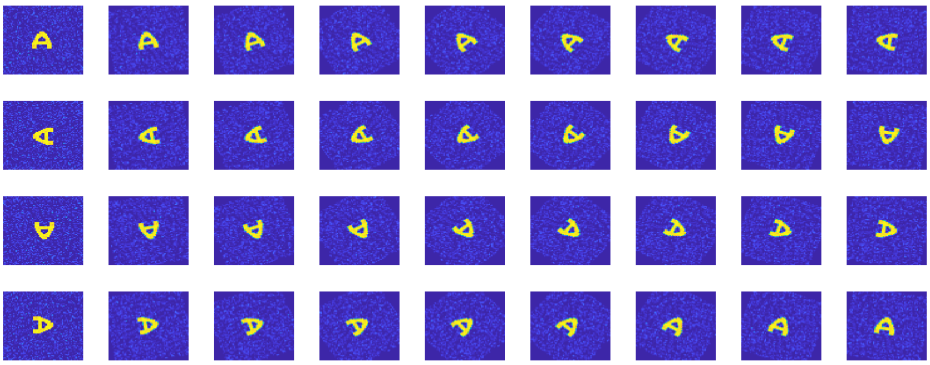

Figure 3.4: Rotations of the capital letter A. The rotation increases with 10 degrees and thus results in 36 separate files for each letter. Gaussian noise can also be seen in these images.

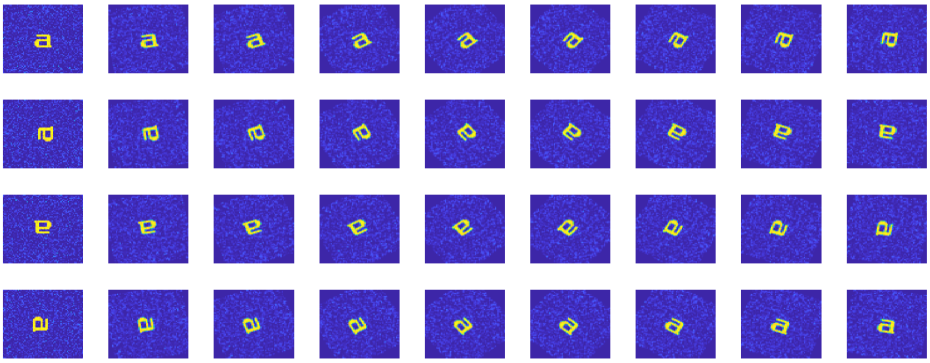

Figure 3.5: Rotations of the small letter a. The rotation increases with 10 degrees and thus results in 36 separate files for each letter. Gaussian noise can also be seen in these images.

3.2.2. Data

The data described in the first section of this chapter is also used for the deep learning in this project. Gaussian noise with a variance of $2.2 * 10^{-5}$ is added to the images to ensure the background is not completely homogeneous. A common problem for deep learning, as discussed in Section 2.6, is the size of the data set. The data set consists of twice the alphabet and thus 52 separate images and their corresponding signals. This would, however, not be enough to be able to train a network accurately. Therefore augmentations are performed, all images are rotated 36 times with a rotation angle of 10 degrees resulting in a set per letter as represented in Figure 3.4 and 3.6. This increases the data set from 52 to 1872 separate images and signals. A standard split of 80/20 is used to split this set into a training and a testing set. A batch size of 32 samples and 50 epochs was used for training. A second data set, consisting of the same letters but different rotations, is used as a validation set. This data set consists of 6 rotations per letter and is thus a set of 312 images and corresponding signals. This set will be kept separate from the model during training to ensure that the model can eventually predict on unseen data. An overview of the used data can be seen in Table 3.1.

The signals, consisting of 39963 complex numbers for each letter, are re-scaled to a vector of 79926x1 with all real parts of the original vector followed by all the complex parts. This is due to the input shape the network takes.

Finally, when the model predicts well on the simulated data, the signals of the real measurement will be used for a prediction to see if the model can predict accurately on real data.

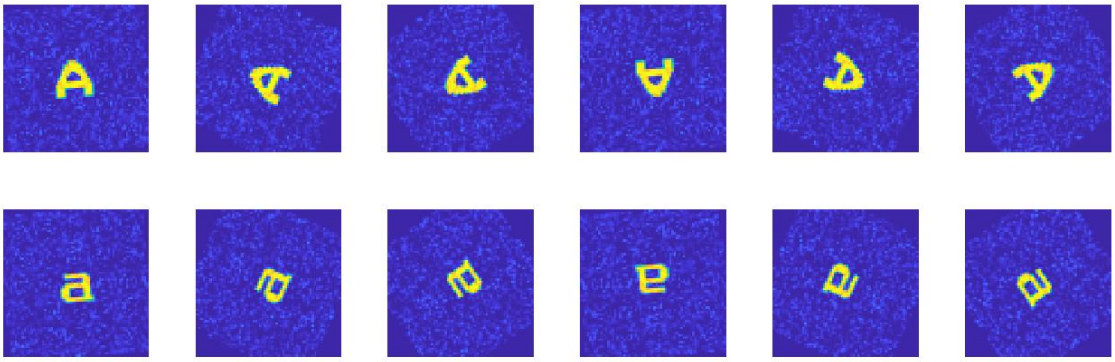

Figure 3.6: Validation set of capital letter A and small letter a. It can be seen that there are 6 rotations for each letter at the orientation of 5, 65, 125, 185, 245 and 305 degrees.

	Train	Test	Validation
Number of samples	1498	374	321
Rotation angles	0 - 360 in steps of 10	0 - 360 in steps of 10	5, 65, 125, 185, 245, 305
Size of input data	79926x1	79926x1	79926x1

Table 3.1: Overview of training, testing and validation data.

4

Results

The results obtained in this research are discussed in this chapter. First the correlations of signals and images are shown (Section 4.1) after which the results of the deep learning are shown (Section 4.2), both on simulated data and on measured data.

4.1. Correlation Signals and Images

Figure 4.1 shows the correlation between every letter and CGLS image reconstruction of the measurement and Figure 4.2 shows the correlation between each letter and the GCGME reconstruction.

In both correlation plots it can be seen that the capital M has a higher correlation between the pixels of the simulation and the measurement. An other thing that can be observed is that the small letters have an overall higher correlation than the capital letters. When viewing the original images in Figures 3.1 and 3.2 it can be seen that the small letters are not only the shape of small letters, they are also smaller size than the capital letters. This results in an intensity concentration in the centre of the image for the small letters which could explain the greater correlation for the measured data also has an intensity concentration in the middle of the image.

Even though minor differences can be seen between the two plots, the shape of the plot corresponds quite a lot. It can be seen that the correlation of the letters with the GCGME is overall a bit higher, but the letters that have a high correlation in one reconstruction method also have a high correlation in the other. This is to be expected as both reconstruction methods result in a similar image as can be seen in Figure 2.10

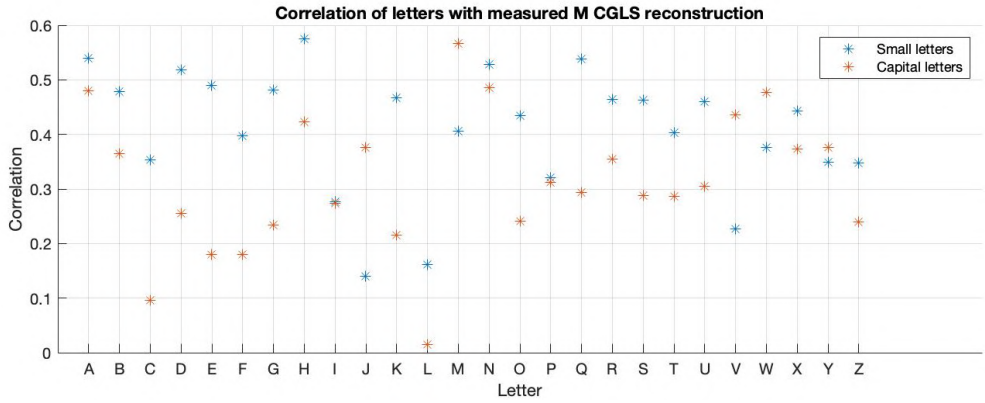

Figure 4.1: Correlation between CGLS reconstructed image and simulated data. It can be seen that while the capital M has a high score (0.5666), the small letter h also had a similar score (0.5744). Overall the small letters have an higher score than the capital letters.

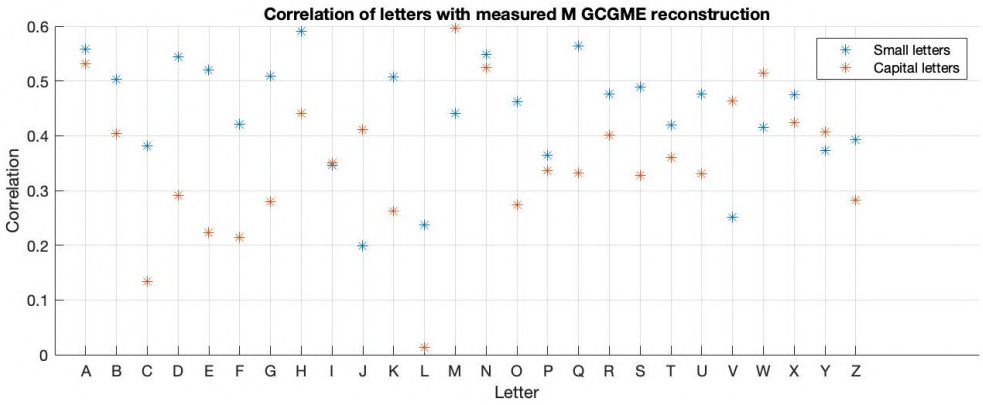

Figure 4.2: Correlation between GCGME reconstructed image and simulated data. It can be seen that while the capital M has a high score (0.5962), the small letter h also had a similar score (0.5906). Overall the small letters have an higher score than the capital letters.

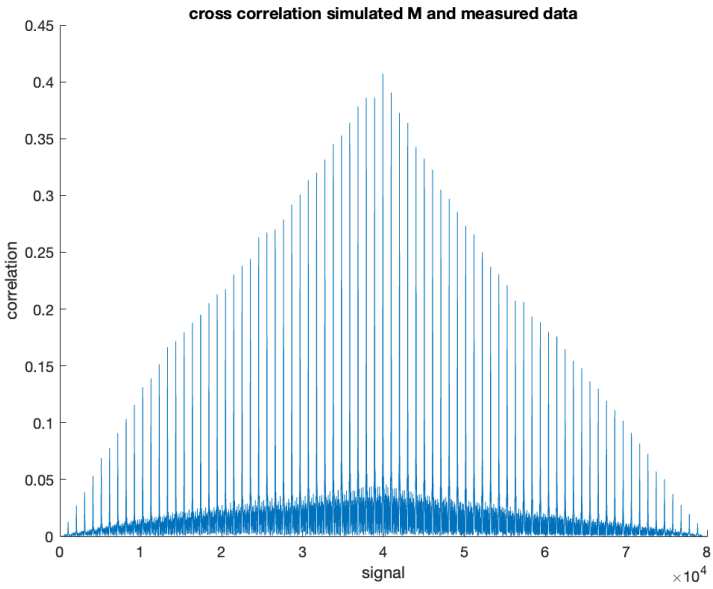

Figure 4.3: Correlation between the measured data and the simulated capital M. It can be seen that the highest peak is the 39th, which corresponds with the amount of translations done. The peak has a height of 0.41.

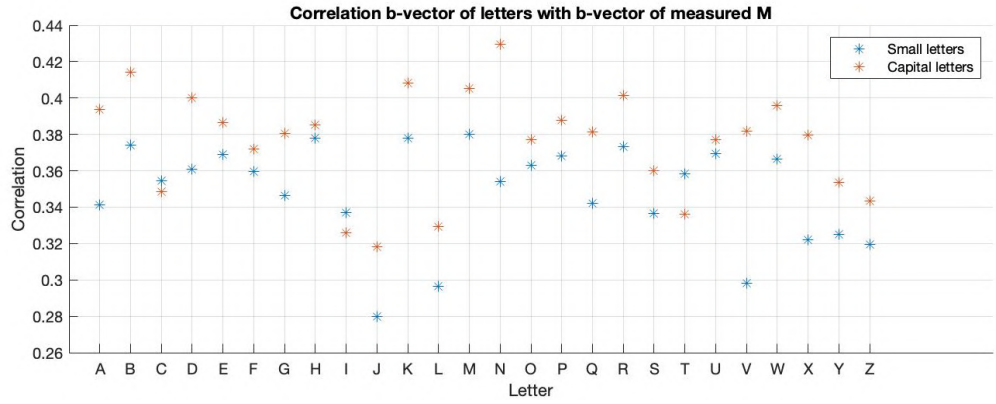

Figure 4.4: Correlation of the measured signals and the simulated signals. It can be seen that the capital letters have an overall higher score than the small letters. The capital B, D, K, M, N and R have a correlation above 0.4 and of these the signal corresponding to the capital N has the highest correlation with the measured signal, at 0.43.

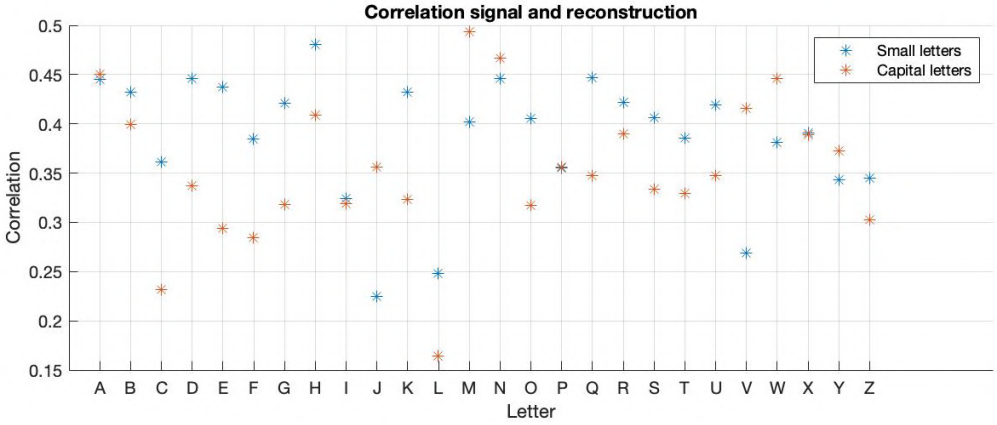

Figure 4.5: Correlation of signals of b-vector and image reconstruction together. It can be seen that the capital M has the greatest overall correlation, at 0.4934.

The correlations between the signals of the measured data and the simulated M are visualised in Figure 4.3. It can be seen that the signal results in an triangular shaped plot consisting of 77 peaks with the highest at the 39th peak which correlates with the amount of translations done in the measurement. The height of this peak represents the greatest correlation between the signals and is just above 0.4. This greatest correlation for all letters can be seen in Figure 4.4. It can be seen that the highest correlation is not the correlation between the measurement and the simulated M, for the capital N has a higher score. It is interesting to note that, for instance, the small letter h, that has a high correlation between the reconstructed images and its simulated image, but does not have a high correlation between the signals.

To be able to visualise such differences, and compare the overall correlation between the measured M and the simulated images and signals, a total correlation is calculated via Equation 3.4 and visualised in 4.5. In this plot it can be seen that when taking all correlations into account the capital M has the greatest correlation with the scanned M.

An overview of all correlations can be found in Appendix B.

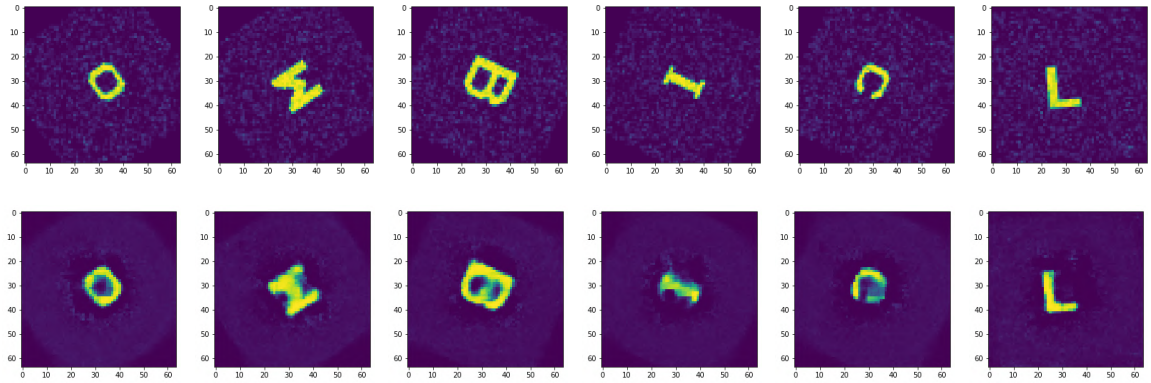

Figure 4.6: **Top Row** : The images of which the signal was used as input for the image reconstruction. **Bottom Row** : The images reconstructed by the algorithm. All images are from the validation set.

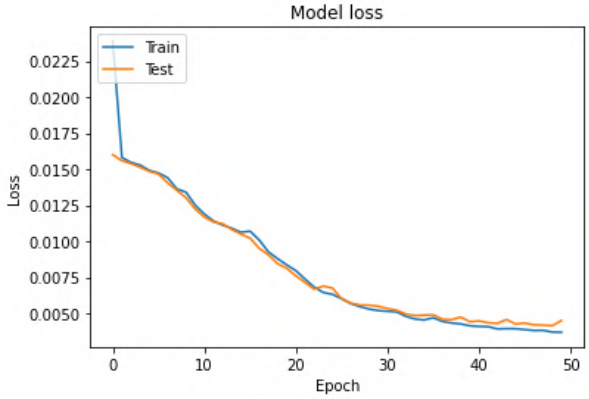

Figure 4.7: Model loss function. It can be seen that after about 40 epochs the loss function reaches an equilibrium of approximately 0.005. The loss function is calculated with the MSE.

4.2. Deep learning

4.2.1. Simulated Data

The reconstruction done by the model explained in Section 3.2.1 of some randomly selected letters can be seen in Figure 4.6, a small o and c and a capital M, B, I and L. These are from the validation data set, which is not used during training and thus unseen data untill prediction. On the top row the ground truth can be seen. These are the images that correspond with the signals that were used as the input for the model. It can be seen that the model is able to reconstruct images in which the original images are recognisable. Figure 4.8 shows the same predictions as Figure 4.6 with in white the boarder of the ground truth as an overlay. These images show that the network is capable to predict images in which the letter is recognisable but they are not pixel perfect.

One thing that stands out is that the borders are more spread out in the predicted images than in the original images. The reconstruction tries to reconstruct images with quite round shapes in the centre of the images. This can, for instance, be seen in the centre of the capital B, in both Figure 4.6 and 4.8, as the model tries to curve the corners inside the B. It can also be seen in the reconstruction of the capital M, also shown in Figure 4.6 and 4.8, in which the corners are not as sharp as the original image.

The loss function, the Mean Squared Error calculated with Equation 3.5 and visualised in Figure 4.7, reduces to an equilibrium around 0.0050.

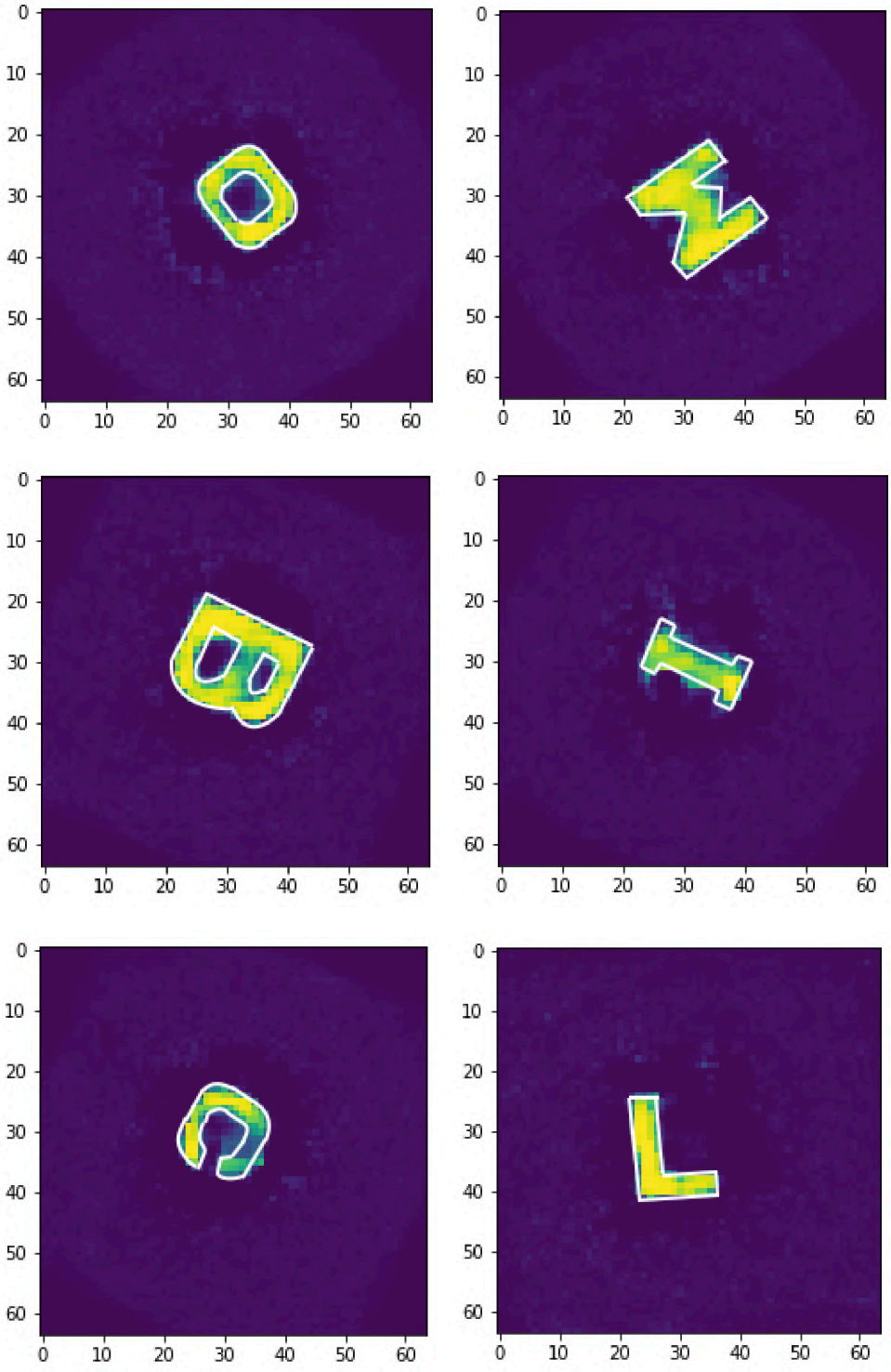

Figure 4.8: The reconstructed images by the model with the borders of the ground truth to visualise the pixel- wise difference between the two.

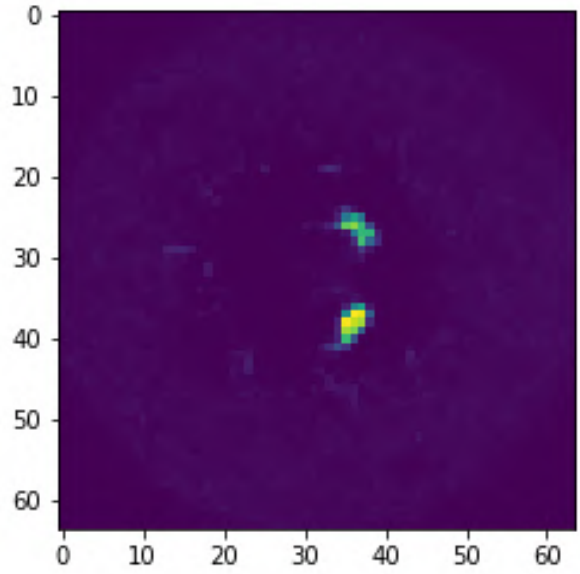

Figure 4.9: Prediction by the AUTOMAP model on measured data after training on simulated data. An M is not recognisable in this reconstruction.

4.2.2. Measured data

A prediction of the measured data presented in Section 2.5.2 was also done by the model presented in this research. The resulting image can be seen in Figure 4.9.

It can be seen that the model does not predict an image similar to the measured and reconstructed data. From this we might assume the model has learned a different way to reconstruction the images than finding the $\mathbf{A}$ from Equation 3.2 for this would result in an image more similar to Figure 2.10. This failed reconstruction might be due to the fact that the data on which the model was trained is quite homogeneous. It is interesting to see that the network predicts some kind of circle in the background. This circle is the corresponds to the background of the simulated data. This shape is due to the rotations done after adding noise to the image.

Due to the lack of real data it was not possible to train the network on real data before prediction, which might have resulted in better predictions. This is discussed further in the next Section.

5

Discussion and Conclusions

While the correlation between the measured data and the simulated data and the prediction results suggests a prediction should be possible on real data, the final prediction on real data seems somewhat disappointing. This chapter will discuss the research, results, and possible future improvements.

5.1. Discussion

Section 4.1 suggests a correlation between the measured signals and simulations of the same shape. However, even though the correlation between these signals and images is higher than the correlation between simulations that are not the correct shape, such as a capital N or a small h, the difference is not significant. When viewing the reconstructed images, the capital M has the highest correlation. However, when inspecting the signals, it can be seen that the signal corresponding to the capital N is higher than the capital M. Since only the signals were taken into account for deep learning, it could be suggested that the information embedded in the signals is not enough for accurate image prediction.

Another thing to consider is that only one measurement is used for these correlations, for only one was available. Only the correlation between the real measurement of the M and other letters could be checked. It would be very interesting to see if real measurements of other letters would also have a more significant correlation to the simulation of that letter. Due to practical hurdles, it was impossible to take measurements of other letters. As this correlation is the basis of the hypothesis that the information needed for image reconstruction is embedded in the signal, it would be good to check this correlation with other letters.

At the start of the project, it was planned to do more real measurements with the scanner to create a data set on which the network could train; however, due to some setbacks, this was not possible. The scanner in which the measurements were done 2021 in Leiden was moved to Delft. The time between the measurements and the move was more than four months. During this move, a wire broke, which led to a setback in the schedule. The wire had been fixed by autumn, and measurements could be done in Delft. However, due to the combination of the circuit and the resistors with the RF amplifier of the previous low-field MRI set-up, the wires in the scanner burned after one scan resulting in measurements in which nothing was visible. After reconfiguring the circuit in the scanner, incorporating higher resistors and reducing the output of the RF amplifier, measurements were finally possible. A problem during reconfiguration was that the person responsible for building the scanner had withdrawn himself from the project. He had the most knowledge of the circuit and the magnet but could not help in reconfiguration. By the time the scanner was working, it was the spring of 2022. The sample inside the scanner had been in the scanner for more than half a year. As the sample was filled with only a few drops of oil and the scanner had been moved twice, from Leiden to Delft and within Delft again, the oil had started leaking. Due to the set-up of the scanner, it is not easily possible to replace the sample, for the coil is wrapped around and glued to the sample. When removing the sample from the coil and adding a new one, the configuration of the circuit must also be reevaluated. Due to the time limit in this project, the sample was therefore not replaced. Results of measurements do not show the M that was scanned, as can be seen in Appendix A but result only in visualising the coil sensitivity.

Inspecting the data set used, one of the first things that stands out is that the data set is relatively

homogeneous. While Gaussian noise is added, the letters have the same intensity, and the background is also relatively homogeneous. All letters are positioned in the same location in the image, with a large border around them. While this border was based on the real measurement, it could be possible that the network concentrates too much on predicting the background instead of the letter itself. In future projects, this can be compensated by prioritising the prediction in the centre of the image by penalising this area more in the loss function.

Furthermore, the data set used in this project was constructed with a background of Gaussian noise. However, the background is not homogeneous in the data scanned with the handheld low-field scanner because it has a field strength gradient. For future research, it would be interesting to see if the predictions on real data would improve if this gradient were incorporated into the background of the simulated training data.

Besides the fact that the training data is relatively homogeneous, a lack of real data was also a problem in this project. Due to practical hurdles concerning the handheld scanner mentioned earlier, it was not possible to do more measurements within the time frame of this project. It would have been possible to train the model on real data via transfer learning before prediction with more data and might have resulted in a better prediction on the real data as it has in previous projects [15] [19].

5.2. Conclusion

This report examined if deep learning-based image reconstruction can improve image reconstruction for a low-field handheld MRI scanner?

Investigation into the correlations between simulated data and the real measured data shows a more significant correlation between the measurement and the simulated M than with other simulated letters. However, when viewing the image reconstruction via deep learning for the low-field handheld scanner, the predictions on the real data are not accurate yet, even though the predictions on the simulated data show potential. With more real measurements to train the model on, a less homogeneous background for the simulated data and innovative penalties to focus the model on a prediction in the centre of the image, it could be possible to reconstruct real measured data with the handheld low-field MRI scanner in the future.

Bibliography

[1] Felix Bloch. “Nuclear induction”. In: *Physical review* 70.7-8 (1946), p. 460.

[2] B Blümich et al. “The NMR-mouse: construction, excitation, and applications”. In: *Magnetic resonance imaging* 16.5-6 (1998), pp. 479–484.

[3] Jorge Zavala Bojorquez et al. “What are normal relaxation times of tissues at 3 T?” In: *Magnetic resonance imaging* 35 (2017), pp. 69–80.

[4] Merel de Leeuw den Bouter et al. “Description of a Low-field MRI Scanner Based on Permanent Magnets.” In: *CEUR Workshop Proceedings* 2688.15 (2020).

[5] Merel L de Leeuw den Bouter, Martin B van Gijzen, and Rob F Remis. “Conjugate gradient variants for ℓp-regularized image reconstruction in low-field MRI”. In: *SN Applied Sciences* 1.12 (2019), pp. 1–15.

[6] Robert W Brown et al. *Magnetic resonance imaging: physical principles and sequence design*. John Wiley & Sons, 2014.

[7] Roel Burgwal. *Measuring NMR and developing 2D imaging in a low-cost, portable MRI prototype*. Msc. Thesis. Delft University of Technology, 2018.

[8] F Casanova and B Blümich. “Two-dimensional imaging with a single-sided NMR probe”. In: *Journal of Magnetic Resonance* 163.1 (2003), pp. 38–45.

[9] Govind B Chavhan et al. “Principles, techniques, and applications of T2*-based MR imaging and its special applications”. In: *Radiographics* 29.5 (2009), pp. 1433–1449.

[10] Clarissa Zimmerman Cooley et al. “Two-dimensional imaging in a lightweight portable MRI scanner without gradient coils”. In: *Magnetic resonance in medicine* 73.2 (2015), pp. 872–883.

[11] Kristen Coyne. “MRI: A guided tour”. In: *MagLab.< https://nationalmaglab. org/education/magnet-academy/learn-the-basics/stories/mri-a-guidedtour> January* (2015). retrieved September 2021.

[12] Raymond Damadian. “Tumor detection by nuclear magnetic resonance”. In: *Science* 171.3976 (1971), pp. 1151–1153.

[13] Jeffrey A. Fessler. “Model-Based Image Reconstruction for MRI”. In: *IEEE Signal Processing Magazine* 27.4 (2010), pp. 81–89. DOI: 10.1109/MSP.2010.936726.

[14] Amanda K Funai et al. “Regularized field map estimation in MRI”. In: *IEEE transactions on medical imaging* 27.10 (2008), pp. 1484–1494.

[15] Dilan Geçmen. *Deep Learning Techniques for Low-Field MRI*. Msc. Thesis. 2020.

[16] Mason Greer, Cheng Chen, and Soumyajit Mandal. “An easily reproducible, hand-held, single-sided, MRI sensor”. In: *Journal of Magnetic Resonance* 308 (2019), p. 106591.

[17] Klaus Halbach. “Design of permanent multipole magnets with oriented rare earth cobalt material”. In: *Nuclear instruments and methods* 169.1 (1980), pp. 1–10.

[18] Zhonghua He et al. “The novel design of a single-sided MRI probe for assessing burn depth”. In: *Sensors* 17.3 (2017), p. 526.

[19] Armando Garcia Hernandez et al. “Improving Image Quality In Low-Field MRI With Deep Learning”. In: *2021 IEEE International Conference on Image Processing (ICIP)*. IEEE. 2021, pp. 260–263.

[20] ML de Leeuw den Bouter. *Image Reconstruction for Low-Field MRI*. Doctoral Thesis. Delft University of Technology, 2022.

[21] Dana J Lin et al. “Artificial intelligence for MR image reconstruction: an overview for clinicians”. In: *Journal of Magnetic Resonance Imaging* 53.4 (2021), pp. 1015–1028.

[22] José P Marques, Frank FJ Simonis, and Andrew G Webb. “Low-field MRI: An MR physics perspective”. In: *Journal of magnetic resonance imaging* 49.6 (2019), pp. 1528–1542.

[23] MA Martens et al. “Insertable biplanar gradient coils for magnetic resonance imaging”. In: *Review of scientific instruments* 62.11 (1991), pp. 2639–2645.

[24] Patrick C McDaniel et al. “The MR cap: A single-sided MRI system designed for potential point-of-care limited field-of-view brain imaging”. In: *Magnetic resonance in medicine* 82.5 (2019), pp. 1946–1960.

[25] “Nobel Prize in Physics”. In: *Physics Today* 5.12 (1952), pp. 22–22. DOI: 10.1063/1.3067428.

[26] Anna Nowogrodzki. “The world’s strongest MRI machines are pushing human imaging to new limits.” In: *Nature* 563.7732 (2018), pp. 24–27.

[27] A. Van Oosterom and T.F. Oostendorp. *Medische Fysica*. Bohn Stafleu van Loghum, 2001.

[28] Pieter Oppelaar. *Model based image reconstruction for low-field hand-held MRI: On imaging using field geometry and sample translations*. Bsc. Thesis. 2021.

[29] J Perlo, F Casanova, and B Blümich. “3D imaging with a single-sided sensor: an open tomograph”. In: *Journal of Magnetic Resonance* 166.2 (2004), pp. 228–235.

[30] Donald B Plewes and Walter Kucharczyk. “Physics of MRI: a primer”. In: *Journal of magnetic resonance imaging* 35.5 (2012), pp. 1038–1054.

[31] Sertan Serte, Ali Serener, and Fadi Al-Turjman. “Deep learning in medical imaging: A brief review”. In: *Transactions on Emerging Telecommunications Technologies* (2020), e4080.

[32] Nahian Siddique et al. “U-net and its variants for medical image segmentation: A review of theory and applications”. In: *IEEE Access* (2021).

[33] Jian Wang et al. “A review of deep learning on medical image analysis”. In: *Mobile Networks and Applications* 26.1 (2021), pp. 351–380.

[34] Bo Zhu et al. “Image reconstruction by domain-transform manifold learning”. In: *Nature* 555.7697 (2018), pp. 487–492.

A

Appendix: Measurements Delft

The handheld MRI scanner was moved from the LUMC to the TU Delft in the fall of 2021. During this move, parts of the wiring in the scanner broke. After repair, the first measurements were taken. However, due to the hardware configuration of the original measurement in Leiden, the settings used were not known. This included the amplitude of the RF pulse used in Leiden. When the first measurements were done, the RF amplitude for the highest response pulse thus had to be estimated. Measurements with different RF amplitudes were taken, of which some different signals can be seen in Figure A.1. In these measurements, a peak cannot be seen, but after some testing, an RF amplitude of 0.6 seemed to give a small peak, as can be seen in Figure A.2. However, an offset can be seen throughout the imaginary and real part of the signal. The signal is expected to be centred around 0 but has an offset below 0.

The offset was removed by adding the absolute of the mean of the measurement to each point.

$$b = |\overline{b}| + b \tag{A.1}$$

in which b is the received signal and $\overline{b}$ is the average of this signal. This results in the signals as seen in Figure A.3 in which the top row shows the original data that is not centred around 0. The bottom row represents the measurement after correcting for the offset, and it can be seen that the data now oscillates around 0.

A new measurement was conducted with the same translations as used for the measurement in Leiden (visualised in Figure 2.8). The image is reconstructed using the image reconstruction explained in Section 2.3.3 and the images are visualised in Figure A.4. An M can not be seen in the reconstruction; a cross is visible. This can be explained when realising the shape of the cross corresponds with the coil sensitivity at depth $z = 28,5$. What is visualised in this image is the shape of where the scanner is more likely to pick up the signal; for more information, see [20]. Much time had passed between the original measurements and when the measurements in Delft were conducted. The oil in the sample may have leaked into the container. Since only a few drops of oil are inside the sample, some leaking or smearing can already influence the measurement. Due to how the scanner is built, it is not possible to replace only the sample without replacing the coil, which, in its turn, leads to a reconfiguration of the complete circuit. Therefore, it was not possible to replace and improve this within the time limit of this project.

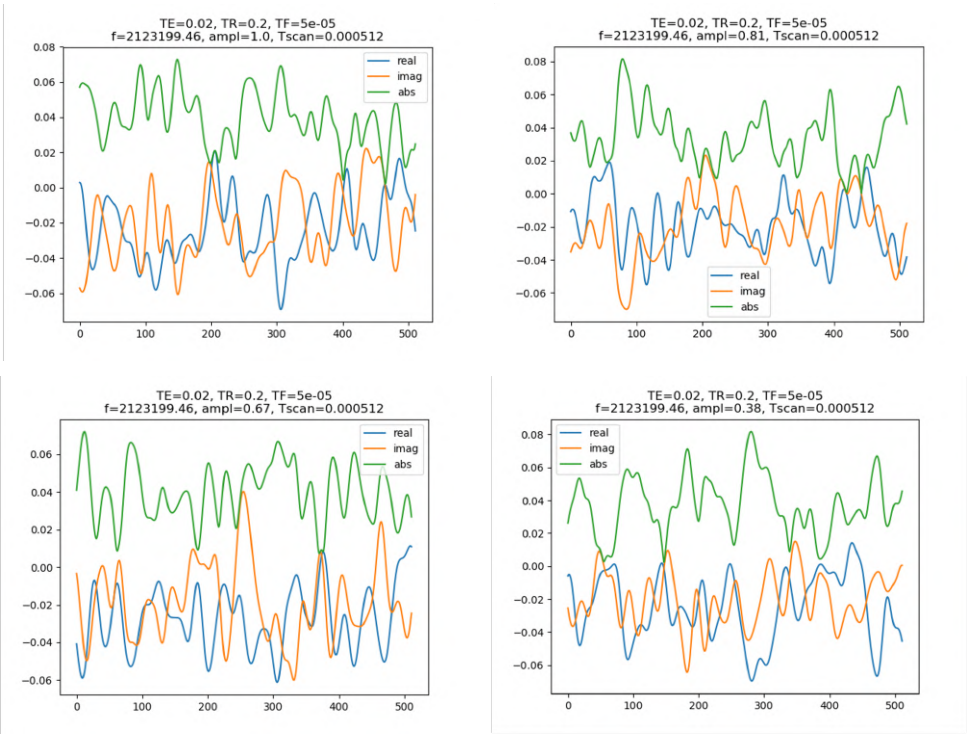

Figure A.1: Signal response from single measurements done in Delft. An offset can be seen as the real and imaginary part is expected to be centred around 0.

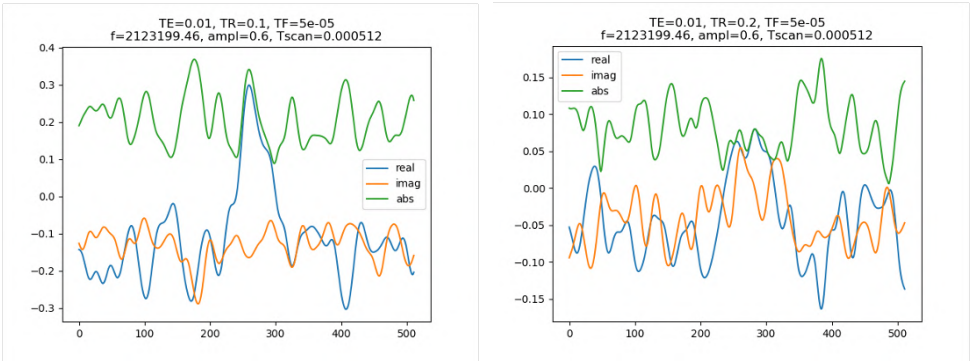

Figure A.2: After investigation the correct RF amplitude is found at 0.6. This results in single signal plots, seen in this figure. An offset can be seen as the real and imaginary part is expected to be centred around 0.

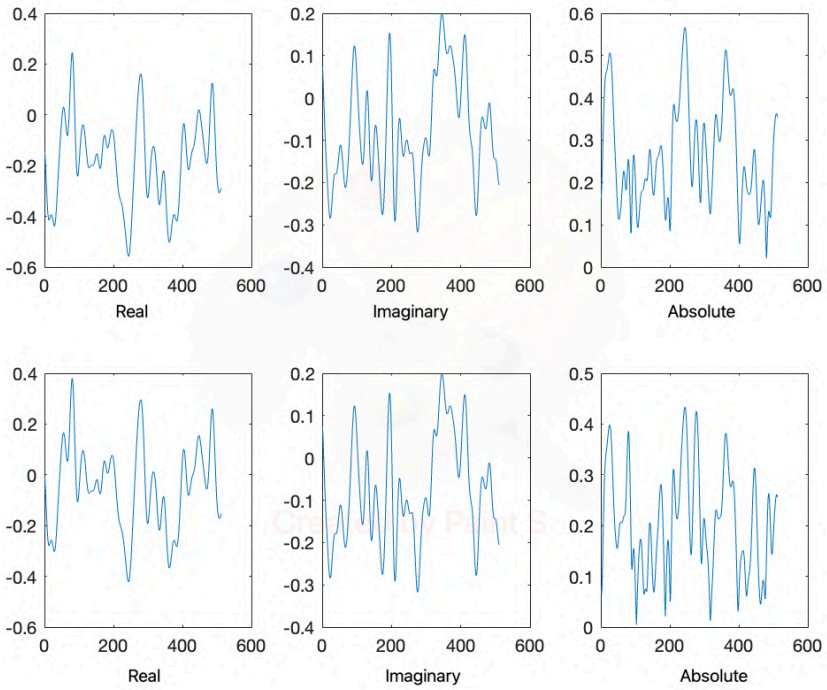

Figure A.3: **Top Row**: The original measurement can be seen split into real, imaginary and the absolute of the measurement. An offset can be seen in the real and the imaginary part. The measurement shown is the first translation of the total measurement and thus consists of 512 data points. **Bottom Row**: The same measurement as in the top row is visualised but the offset is corrected. It can now be seen that the measurement oscillates around 0.

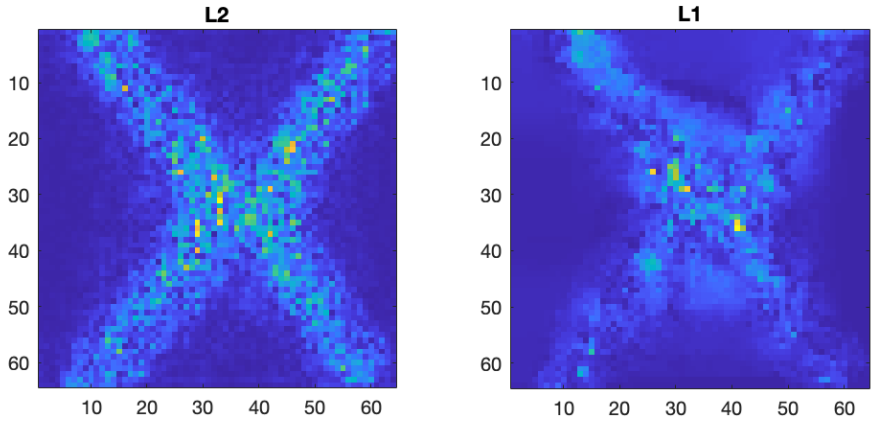

Figure A.4: Image reconstruction of measurements in Delft. **Left**: Image reconstruction done via CGLS. **Right**: Image reconstruction done via GCGME. The CGLS reconstruction seems to be similar to the coil sensitivity at $z = 28,5mm$.

B

Appendix: Correlations overview

Letter	Signal	GCGME reconstruction	CGLS reconstruction	Reconstruction + signal
a	0.3415	0.5583	0.5389	0.4450
b	0.5030	0,4143	0.4782	0.4324
c	0.3544	0.3813	0.3532	0.3609
d	0.5444	0,4001	0.5176	0.4460
e	0.3690	0.5202	0.4905	0.4372
f	0.3597	0.4216	0.3970	0.3845
g	0.3462	0.5085	0.4817	0.4207
h	0.3778	0.5906	0.5744	0.4802
i	0.3372	0.3459	0.2772	0.3244
j	0.2798	0.1992	0.1395	0.2246
k	0.3778	0.5068	0.4676	0.4325
l	0.2964	0.2370	0.1617	0.2479
m	0.3800	0.4409	0.4064	0.4018
n	0.3540	0.5485	0.5288	0.4464
o	0.3630	0.4614	0.4339	0.4053
p	0.3680	0.3641	0.3203	0.3551
q	0.3420	0.5640	0.5381	0.4465
r	0.3734	0.4759	0.4643	0.4218
s	0.3366	0.4888	0.4627	0.4061
t	0.3584	0.4202	0.4034	0.3851
u	0.3695	0.4768	0.4598	0.4189
v	0.2980	0.2514	0.2272	0.2687
w	0.3664	0.4148	0.3765	0.3810
x	0.3222	0.4747	0.4430	0.3905
y	0.3249	0.3732	0.3493	0.3431
z	0.3197	0.3924	0.3482	0.3450

Table B.1: Correlations overview for small letters.

Letter	Signal	GCGME reconstruction	CGLS reconstruction	Reconstruction + signal
A	0.3938	0.5318	0.4805	0.4500
B	0.4143	0.4038	0.3650	0.3994
C	0.3484	0.1340	0.0962	0.2317
D	0.4001	0.2908	0.2559	0.3367
E	0.3864	0.2224	0.1798	0.2938
F	0.3721	0.2141	0.1797	0.2845
G	0.3806	0.2790	0.2335	0.3184
H	0.3850	0.4414	0.4235	0.4087
I	0.3259	0.3500	0.2739	0.3189
J	0.3182	0.4116	0.3755	0.3559
K	0.4082	0.2619	0.2152	0.3234
L	0.3291	0.0128	0.0147	0.1641
M	0.4054	0.5962	0.5666	0.4934
N	0.4294	0.5249	0.4849	0.4671
O	0.3771	0.2736	0.2409	0.3172
P	0.3877	0.3357	0.3117	0.3557
Q	0.3814	0.3317	0.2938	0.3471
R	0.4012	0.4007	0.3547	0.3895
S	0.3598	0.3274	0.2872	0.3336
T	0.3362	0.3596	0.2863	0.3296
U	0.3770	0.3304	0.3053	0.3474
V	0.3817	0.4631	0.4361	0.4156
W	0.3958	0.5139	0.4776	0.4458
X	0.3797	0.4240	0.3735	0.3892
Y	0.3537	0.4063	0.3761	0.3725
Z	0.3434	0.2828	0.2401	0.3024

Table B.2: Overview of correlations for capital letters.